

# Fabrication Strategies of Twisted Bilayer Graphenes and Their Unique Properties

Le Cai and Gui Yu\*

Twisted bilayer graphene (tBLG) exhibits a host of innovative physical phenomena owing to the formation of moiré superlattice. Especially, the discovery of superconducting behavior has generated new interest in graphene. The growing studies of tBLG mainly focus on its physical properties, while the fabrication of high-quality tBLG is a prerequisite for achieving the desired properties due to the great dependence on the twist angle and the interfacial contact. Here, the cutting-edge preparation strategies and challenges of tBLG fabrication are reviewed. The advantages and disadvantages of chemical vapor deposition, epitaxial growth on silicon carbide, stacking monolayer graphene, and folding monolayer graphene methods for the fabrication of tBLG are analyzed in detail, providing a reference for further development of preparation methods. Moreover, the characterization methods of twist angle for the tBLG are presented. Then, the unique physicochemical properties and corresponding applications of tBLG, containing correlated insulating and superconducting states, ferromagnetic state, soliton, enhanced optical absorption, tunable bandgap, and lithium intercalation and diffusion, are described. Finally, the opportunities and challenges for fabricating high-quality and large-area tBLG are discussed, unique physical properties are displayed, and new applications inferred from its angle-dependent features are explored, thereby impelling the commercialization of tBLG from laboratory to market.

## 1. Introduction

Graphene, a single atomic layered carbon material with honeycomb structure, has attracted broad prospects in optoelectronic devices because of its excellent electrical, optical, magnetic, mechanical properties, and stable chemical properties.<sup>[1–5]</sup> Moreover, graphene has a promoted function in energy storage and conversion due to the good electrical conductivity, large surface area, and the isolation capability for oxygen and

water.<sup>[6–8]</sup> Therefore, graphene becomes a rising star on the horizon of materials science. Since the first report of centimeter-scale single-crystal graphene by Ruoff group showed high electrical quality,<sup>[9]</sup> great achievements have been made in the fabrication of high-quality graphene for the application in electronic devices, including single-crystalline graphene flakes,<sup>[10,11]</sup> super-ordered graphene structures,<sup>[12,13]</sup> super-clean graphene films,<sup>[14–16]</sup> and ultra-flat graphene films.<sup>[17]</sup> However, the zero-bandgap feature for monolayer graphene has limited its potential applications in semiconductors. In addition, the negligible mass, low yield, and high production costs of graphene are insurmountable bottlenecks for the practical application in energy conversion and storage. In particular, the absence of killer applications leads to the increased difficulty in graphene commercialization.<sup>[18,19]</sup> Nevertheless, it is undeniable that the unique structure of graphene has sparked intense interest in condensed matter physics, such as fractional quantum Hall effects,<sup>[17]</sup> proton permeation,<sup>[20]</sup> and plasmons.<sup>[21]</sup> More interestingly, twisted bilayer graphene (tBLG), which is similar to the van der Waals heterostructures, has a dramatic effect on the electronic properties.<sup>[22,23]</sup> The relative rotating graphene layers become a powerful model to study topological physical properties, including ferromagnetism,<sup>[24]</sup> Mott insulating behavior and superconducting behaviors,<sup>[25,26]</sup> topological valley transport,<sup>[27]</sup> van Hove singularities,<sup>[28]</sup> and tunable bandgap.<sup>[29]</sup> Consequently, the twisted structure of tBLG has triggered tremendous enthusiasm, even inspiring the formation of a new field for twisted 2D materials.

Currently, production methods of tBLG contain chemical vapor deposition (CVD) on metal catalysts;<sup>[30]</sup> epitaxial growth on SiC substrate;<sup>[31]</sup> folding monolayer graphene,<sup>[32]</sup> and stacking monolayer graphene.<sup>[33]</sup> These methods are divided into two categories: direct growth and manual assembly. Generally, the direct growth of tBLG undergoes an *in situ* rearrangement of carbon atoms in the non-equilibrium state at high temperatures, whereas the *ex situ* vertical overlap of monolayer graphene by transfer process is the basic principle for manual assembly. The completely different preparation processes give rise to the distinctive advantages and disadvantages, but precise control over twist angle and super-clean interface are the ultimate pursuits for any preparation method. Recent progress in

L. Cai, Prof. G. Yu  
 Beijing National Laboratory for Molecular Sciences  
 CAS Research/Education Center for Excellence in Molecular Sciences  
 Institute of Chemistry  
 Chinese Academy of Sciences  
 Beijing 100190, P. R. China  
 E-mail: yugui@iccas.ac.cn  
 L. Cai, Prof. G. Yu  
 School of Chemical Sciences  
 University of Chinese Academy of Sciences  
 Beijing 100049, P. R. China

The ORCID identification number(s) for the author(s) of this article can be found under <https://doi.org/10.1002/adma.202004974>.

DOI: 10.1002/adma.202004974

fabrication of tBLG is much slower than monolayer graphene because of the increased difficulty in control over twisted structures. The lattice structure, band structure, and physical properties change dramatically with twist angle and interfacial contact.<sup>[34]</sup> As a result, the preparation methods of tBLG urgently need to be summarized for guiding the development of high-quality and diverse twisted graphene.

In short, great progress on tBLG has been achieved by numerous excellent studies in recent years. Although a few reviews on its physical properties have been reported,<sup>[35–37]</sup> the systematical introduction and summary for the fabrication challenges and preparation strategies of tBLG, characterization methods of twist angle, and their unique physicochemical properties is still lacking. Herein, we describe the cutting-edge preparation methods of tBLG and analyze their features and drawbacks to disclose the influence in properties and application of tBLG. Moreover, we summarize the methods for estimating twist angle of the tBLG. Then, we review unique physicochemical properties and corresponding applications of tBLG, containing correlated insulating and superconducting states, ferromagnetic state, soliton, enhanced optical absorption, tunable bandgap, and lithium intercalation and diffusion. Finally, we provide an outlook for the formation of tBLG with precise control over twist angle and the potential application in energy storage and electronic switching devices, aiming to seek a killer application with suitable preparation method for the commercialization of tBLG.

## 2. The Structural Features of tBLG

The mutual rotation of two graphene layers forms the tBLG (**Figure 1a**), generating a periodic Moiré superlattice owing to the strong interface coupling.<sup>[38]</sup> The Moiré superlattice with extended unit cells brings about the variation of local stacking order of carbon atoms to AA/AB/BA modes. Moreover, the size and range of unit cells are directly affected by the twist angle in turn to adjust the local stacking order (**Figure 1b**).<sup>[39]</sup> Herein, the superlattice structure of tBLG can be regarded as the rotation of AB stacked bilayer graphene around an axis with a certain A1B2 point, where A1 and B2 stand for the sublattice for top and bottom graphene layers, respectively (**Figure 1c**).<sup>[40]</sup> The relative rotation changes the electronic band structure, which is different from that of monolayer graphene or AA stacking bilayer graphene. In tBLG, the electronic structure is redistributed: near the Fermi surface, it is a linear distribution the same as that of monolayer graphene; whereas, near the charge neutrality point, the band is modulated to become flat and the Dirac points are separated along K and K' direction (**Figure 1d**). Under the action of separation, the low-energy van Hove singularities (VHS) are formed in the middle of Dirac points (**Figure 1e**).<sup>[38,41]</sup> Besides, in the superlattice of tBLG, there are two types of commensurate structures where the different superlattice Dirac points appear. The six new superlattice Dirac points were observed in the sublattice exchange odd structure, and ten superlattice Dirac points were observed in the sublattice exchange even structure (**Figure 1f,g**).<sup>[42]</sup> These unique features are ascribed to the interactions of electrons and Dirac cones in Moiré superlattice.

However, the interface decoupling without interaction could be observed in tBLG under some conditions, which behaves as two monolayer graphene. The transformation is related to the growth substrate and the interface distance. For example, the 30°-tBLG grown on the Pt(111) substrate had the mirrored Dirac cones and an opened bandgap.<sup>[43]</sup> A weaker and additional contour occurred at the reflected position of Brillouin zone (BZ) for 0°-graphene layer with respect to the BZ edges of 30°-graphene layer (**Figure 1h,i**), suggesting the spatial overlaps and interaction between graphene layers. Besides, the bandgap opening occurred at the M point of 30°-graphene layer and changed with the distance away from the M point, showing a coherent scattering process originated from the strong interlayer coupling (**Figure 1j**). The general coupling condition of tBLG is the following formula:

$$k_1^u = k_2^u - G^u + G^d \quad (1)$$

where  $k_1^u$  and  $k_2^u$  are the wave vectors for two Bloch states in one graphene layer,  $G^u$  and  $G^d$  are the reciprocal lattice vectors in the same graphene layer and its counterpart. However, 30°-tBLG grown on Cu(111) substrate behaved as the overlap of two monolayer graphene and the linear electron dispersion relation is retained.<sup>[44]</sup> The Fermi velocity in this 30°-tBLG approached to that of single layer graphene, and the degeneracy factor was twice that of the monolayer graphene (**Figure 1k,l**). These results are attributed to the non-modification of electronic band structure derived from the interlayer decoupling. Furthermore, the interlayer decoupling at other twist angles can be implemented by tuning the interlayer distance.<sup>[45]</sup> The decoupling distance is different and depends on the twist angle. The decrease in twist angle leads to a higher decoupling distance. Thus, tBLG with a smaller angle is of great significance for both fundamental scientific research and potential commercial application due to the strong interlayer coupling.

## 3. The Manufacturing Techniques of tBLG

The research on electronic structure of tBLG is traced back to a decade ago,<sup>[46]</sup> but the development of preparation methods for tBLG is lagging because of the higher difficulty compared to the formation of monolayer graphene. Lately, the explorations of physical properties for tBLG disclose its high dependence on the twist angle.<sup>[47]</sup> However, the manufacturing techniques of tBLG with fine control over twist angle face a great challenge. Inspired by the structure of tBLG, the vertical stacking of two monolayer graphene by manual assembly is the simplest way, and the assembly of 2D van der Waals heterostructures provides the relevant experiences. Also, the growth of bilayer graphene on metal or SiC surface offers technical support for the synthesis of tBLG at a high temperature. Several mainstream approaches are listed below, and their features are shown in **Figure 2**.

### 3.1. Chemical Vapor Deposition

The fine control over the thickness, morphology, and size of graphene can be realized by CVD method, and the roll-to-roll

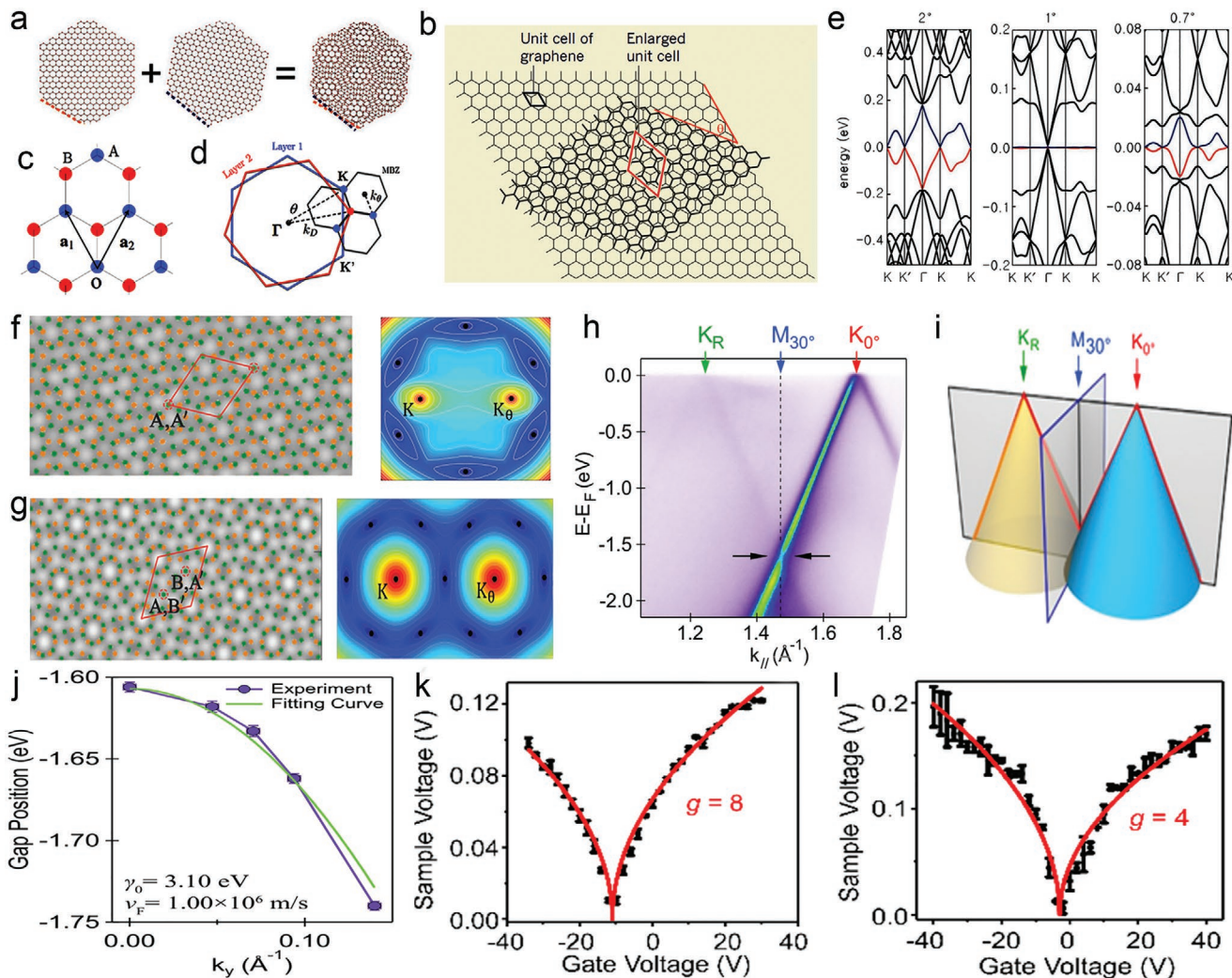


**Figure 1.** The structural features of tBLG. a) Schematic illustration of the formation of tBLG by the vertical overlap of two monolayer graphene with relative rotation. Reproduced with permission.<sup>[38]</sup> Copyright 2017, National Academy of Sciences. b) The enlargement of unit cell at the superlattice of tBLG. Reproduced with permission.<sup>[39]</sup> Copyright 2018, Springer Nature. c) A layer of graphene in tBLG system in the real space. d) The mini Brillouin zone of tBLG in momentum space. c,d) Reproduced with permission.<sup>[40]</sup> Copyright 2018, American Chemical Society. e) The energy band of tBLG with different twist angle. The VHS occurs at the midpoint of K and K'. Reproduced with permission.<sup>[38]</sup> Copyright 2017, National Academy of Sciences. f) Right: schematic illustration of the sublattice exchange odd structure. Left: the corresponding density plots of the energy dispersion. g) Right: schematic illustration of the sublattice exchange even structure. Left: the corresponding density plots of the energy dispersion. The carbon atoms in two graphene layers are represented by the green and orange dots, respectively. f,g) Reproduced with permission.<sup>[42]</sup> Copyright 2013, American Physical Society. h) The Dirac-type dispersion near the K point of the graphene with 0° orientation; the replica Dirac cones are indicated by green arrow. i) Schematic illustration of mirrored Dirac cone under mirror of 30° BZ edges. j) The curves of gap position as a function of the  $k_y$  direction. h-j) Reproduced with permission.<sup>[43]</sup> Copyright 2018, National Academy of Sciences. The profile of Dirac point energy versus gate voltage for k) 30°-tBLG and l) monolayer graphene. k,l) Reproduced with permission.<sup>[44]</sup> Copyright 2020, American Chemical Society.

process urges CVD to be promising in the industrial production of graphene. In recent years, great achievements have been made in the preparation of graphene by CVD, focusing on growth mechanism,<sup>[48–50]</sup> morphology engineering,<sup>[51–53]</sup> Bernal-stacked bilayer,<sup>[54,55]</sup> and single-crystal film.<sup>[56,57]</sup> Based on this, the growth of tBLG by CVD has rich theoretical and experimental support. The rearrangement of carbon atoms to grow tBLG is catalyzed by metal surfaces, including Cu,<sup>[58]</sup> Pt(111),<sup>[59]</sup> Ni,<sup>[60]</sup> and Cu–Ni alloy.<sup>[61]</sup> Owing to the inconsistency of carbon solubility in catalytic substrate, the growth mechanism of tBLG on metal surfaces is different. The growth of graphene on Cu

surface is decided by the self-limiting surface reactions, which tend to grow single-layer graphene due to the low carbon solubility. The key for growth of bilayer on Cu surface is the destruction of self-limiting aspect, including the increased supply of carbon source,<sup>[62]</sup> oxygen-assistance,<sup>[63]</sup> and high hydrogen pressure.<sup>[64]</sup> By contrast, on the substrate with high carbon solubility (Pt and Ni), the carbon atoms can diffuse into the bulk phase of substrate. During cooling process, tBLG is formed through the precipitation of carbon atoms underneath the pre-grown graphene layer.<sup>[65,66]</sup> The modulation of cooling speed and carbon feedstock's concentration has a direct effect on the layer number

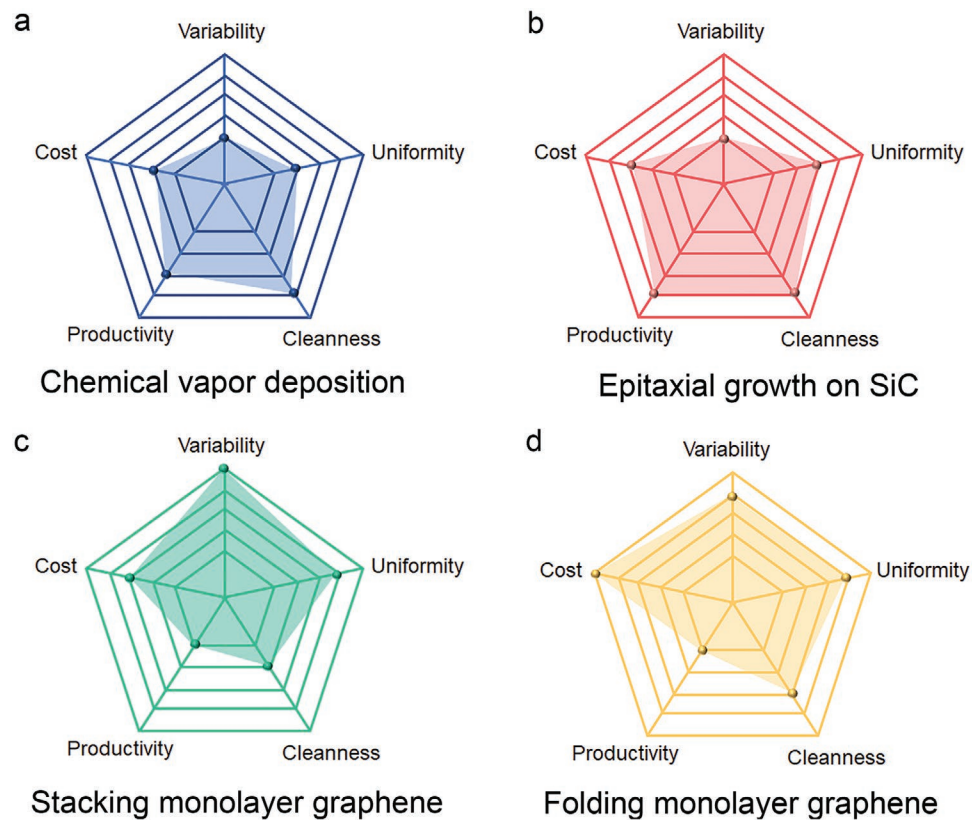


**Figure 2.** Comparison of different preparation methods for tBLG with respect to the variability of twist angle, the uniformity of twist angle, the cleanliness of interface, the productivity, and its production costs. a) Chemical vapor deposition. b) Epitaxial growth on SiC. c) Stacking monolayer graphene. d) Folding monolayer graphene.

and twist angle. As a result, the Cu–Ni alloy which changes the solubility of carbon provides a great platform for the growth of tBLG by controlling the atomic ratio of Ni.

The *in situ* growth allows for tBLG having a clean interface and a relatively high yield in a one-bath process. However, the regulations in grain size and variations in twist angle and layer number remain challenging. Generally, the grain size of tBLG is in the range of tens to hundreds of microns, which is mainly attributed to the different growth rates between top and bottom layer of graphene or non-simultaneous nucleation. Peng et al. reported a two-step process to grow hexagonal tBLG on Cu(111) surface with non-simultaneous nucleation.<sup>[44]</sup> The first graphene layer was deposited on the Cu(111) surface with zigzag or armchair edges due to the highest binding energy. During the first graphene layer growth, the second graphene layer initiated the nucleation through the diffusion of carbon atoms underneath first layer (Figure 3a). Therefore, the second layer was smaller than the first layer owing to the shorter growth time. From photo-electron emission microscopy (PEEM) and micro low energy electron diffraction ( $\mu$ -LEED), the twist angle of bilayer graphene was characterized. There were two types of bilayer regions with exclusive 0°- and 30°-orientations, which were related to the Cu lattice (Figure 3b,c). The 30°-orientation is an incommensurate structure in energy, and its growth relies on the stabilization by Cu(111) substrate. Surprisingly, after being transferred onto SiO<sub>2</sub>/Si substrate or transmission electron microscopy (TEM) grid, tBLG kept the

same orientation and diffraction pattern at a high temperature of 700 °C (Figure 3d,e). The method indicates the possibility of CVD in the synthesis of high quality twisted 2D materials with mass production. Besides, the simultaneous nucleation with different growth rates also leads to the different lateral sizes for two graphene layers. The top layer displays a faster growth rate than that of bottom layer due to the demand of additional energy for the carbon source diffusing from the top layer to the bottom layer.<sup>[67]</sup> On the Cu surface, two layers of graphene in tBLG system are not of the same lateral size and the smaller graphene layer determines the grain size of tBLG. However, Tour et al. developed an interface between Ni foil and SiO<sub>2</sub> to grow large-area tBLG film.<sup>[68]</sup> Owing to the high carbon solubility of Ni layer, the active carbon species diffused into the interface from the top of Ni layer. During the cooling process, a tBLG film with different twist angle was formed on the interface and few layers of graphene on the top of Ni layer. The twist angle changed from 0 to 30° due to the existence of grain boundaries in the graphene layers. Meanwhile, the interface plays an important role for the decline of carbon atoms by diffusion process, providing the constrained environment in favor of the growth of tBLG film.

For the variation in twist angle, the AB stacking with 0°-orientation has the lowest interface energy due to the van der Waals interlayer interaction, which dominates in bilayer graphene or natural graphite crystals.<sup>[69,70]</sup> Although the 30°-misorientation is rarely observed in graphite because of the incommensurate

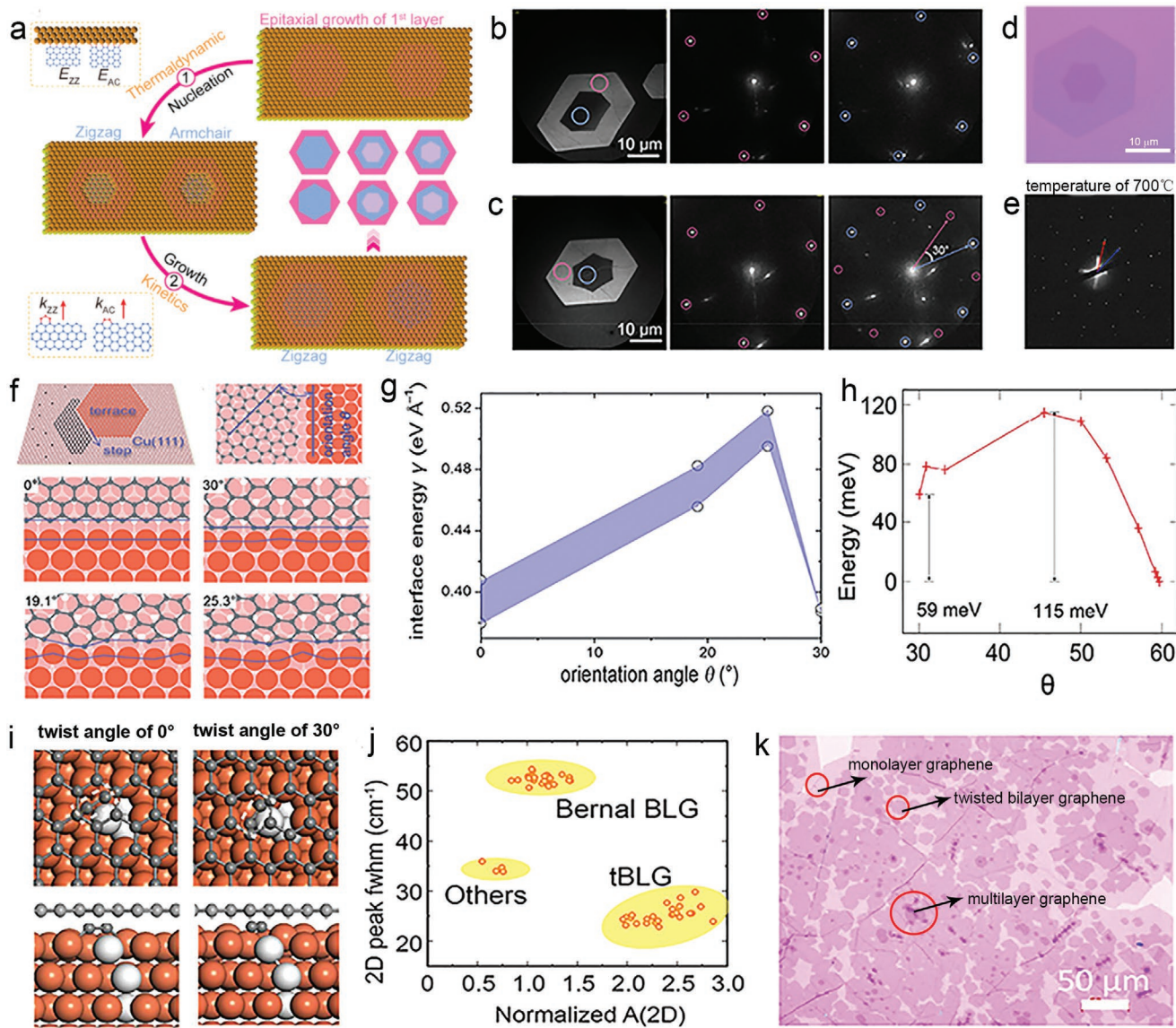


**Figure 3.** The synthesis of tBLG by CVD. a) Schematic illustration of the growth of bilayer graphene under non-simultaneous nucleation process. The PEEM image and  $\mu$ -LEED pattern of b) AB-stacked bilayer graphene and c) 30°-tBLG. d) Optical image of 30°-tBLG after being transferred onto SiO<sub>2</sub>/Si substrate. e) The thermal stability of 30°-tBLG on a TEM grid with heating to 700 °C. a–e) Reproduced with permission.<sup>[44]</sup> Copyright 2020, American Chemical Society. f) Schematic illustration of graphene/Cu(111) step interfaces with different orientation angle. g, h) Reproduced with permission.<sup>[71]</sup> Copyright 2014, Wiley-VCH. h) The curve of energy barrier of the carbon dimer oriented along the zigzag direction (30° in the plot) to armchair direction of graphene (60° in the plot). i) Schematic illustration of the metastable orientation (right) and the stable orientation (left). j) Statistics of stacking mode in bilayer graphene using Raman mapping of the 2D peak normalized. k) Optical image of bilayer graphene grown on Cu-Ni alloy. h–k) Reproduced with permission.<sup>[72]</sup> Copyright 2018, American Chemical Society.

stacking, it is popular in CVD growth process. The preference of 30°-twist angle benefits from the stabilization effect of growth substrate. For instance, Tour group demonstrated that the inter-layer rotation of tBLG was ascribed to the nucleation at the steps on Cu(111) surface.<sup>[71]</sup> The microscopically straight Cu steps were the most stable configuration and offered low-energy sites for bonding C atoms. Hence, the orientation between two graphene layers, which shared the same nucleation site, was determined by the Cu steps. However, why was the 30°-orientation the most prevalent among all the orientations? Clearly, the 30°-orientation rendered a straight graphene edge with armchair configuration,

which could efficiently contact with the Cu step and saturated the dangling bonds. Therefore, the straight interface between armchair edge and Cu step had lower interface energy. On the contrary, other twist angles had rough edges composed of zigzag and armchair segments, which gave rise to the distorted interface between graphene and Cu step. Thus, other twist angles on Cu(111) surface had higher interface energies and were unstable during the growth (Figure 3f,g). However, this model is not appropriate for the Cu–Ni alloy as catalytic substrate due to the different growth mechanisms.<sup>[72]</sup> The introduction of Ni atoms changes the growth mechanism from the self-limiting reaction

into the permeation-diffusion,<sup>[73–75]</sup> and leads to the separation of nucleation site for both the top and bottom graphene layers due to the higher carbon solubility. Consequently, the existence of Ni atoms plays an important role in the secondary nucleation of graphene with different orientations. The formation energy of carbon dimer around Ni atoms displayed a tendency of inverted parabola along armchair direction to zigzag direction of the top graphene layer (Figure 3h). Thus, there were metastable and stable orientations for the growth of 30°-tBLG and Bernal-stacked bilayer graphene, respectively (Figure 3i). Although the 0°- and 30°-stacking orientations are dominant states in CVD-grown bilayer graphene, there are other twist angles.<sup>[76]</sup> The proportional distribution is probably about 48% for Bernal stacking with twist angle of 0°, about 44% for 30°-orientation, and only about 8% for random orientation (Figure 3j).<sup>[71,72]</sup>

For the layer numbers, CVD technique shows great controllability to grow large-area monolayer graphene film on Cu surface or insulated substrates.<sup>[77,78]</sup> However, the synthesis of tBLG encounters the dilemma of inhomogeneous layer thickness, which originates from the increased difficulty in control of carbon source. On the same Cu substrate, there are monolayer, bilayer, and multilayer graphene, showing a decreased proportion and size.<sup>[79,80]</sup> Moreover, monolayer graphene film fully covered on the Cu substrate with adorning small size twisted bilayer flakes is the most universal growth pattern (Figure 3k). In this growth pattern, the graphene film is polycrystalline so that the second graphene layer through grain boundary gives rise to the nonuniformity of twist angle in tBLG.<sup>[81]</sup> The progress on a high selectivity of tBLG is lagging behind. However, the growth of large-area Bernal stacking bilayer graphene has received deep exploration. These include: 1) the high ratio of hydrogen/methane to terminate the graphene edges with hydrogen atom. The detachment of graphene edges from growth substrate promotes the diffusion of active carbon species into the interface for the formation of bilayer graphene with a yield of 99%;<sup>[82]</sup> 2) the designs of high Ni concentration (23%) in Cu–Ni alloy and long growth time for the isothermal growth of bilayer graphene with a yield of 99.4%;<sup>[83]</sup> 3) the use of large-area single-crystal Cu/Ni(111) alloy with Ni concentration of 16.6% for the formation of bilayer graphene with a yield of almost 100%;<sup>[84]</sup> 4) the introduction of ultra-low-limit methane concentration (0.01, 0.03, 0.06, and 0.1%) on Cu–Si alloy to produce a SiC layer, achieving the control of graphene layer number from mono-, bi-, tri-, and tetralayer graphene after the sublimation of Si atoms, respectively.<sup>[85]</sup> Drawing on these strategies, the uniform tBLG was expected to be formed.

Overall, tBLG grown by CVD has a super-clean interface and high productivity due to the numerous nucleation sites in the *in situ* growth process. However, the twist angles concentrate on the 0° and 30°, and the uniformity is affected by the grain boundary. It is worth more exploring in the growth of high-quality and large-area quasicrystal tBLG with variable twist angles consisted of two layers of single crystal graphene.

### 3.2. The Epitaxial Growth on Silicon Carbide

Similar to CVD method, the evaporation of Si atoms and the reconstruction of C atoms on SiC surface offer high-quality

graphene films at extremely high temperatures.<sup>[86]</sup> Moreover, the purposeful treatment for the SiC substrate to build proper crystal surface can regulate the morphology and layer number of graphene.<sup>[87,88]</sup> Thus, tBLG can be successfully prepared on SiC surface via controlling the annealing temperature and time. For instance, Sung et al. exploited hexagonal boron nitride (*h*-BN) as a sacrificial layer to grow tBLG with the millimeter scale.<sup>[89]</sup> By using borazine gas in a vacuum system, a *h*-BN layer was first epitaxially grown on the SiC(0001) substrate, and then the system was heated to a high temperature of 1600 °C to grow first graphene layer in place of the *h*-BN layer. The first graphene layer maintained the 0°-orientation with SiC(0001) substrate under the guidance of the *h*-BN layer. However, the second graphene layer grew between the first graphene layer and the SiC(0001) substrate with an exact rotational angle of 30° due to the absence of *h*-BN layer, which is the general orientation for graphene growth on the SiC surface.<sup>[90]</sup> When the growth temperature for second graphene layer was kept at 1600 °C, tBLG was located on the buffer layer of SiC substrate, while it was located on the hydrogen-terminated SiC substrate at growth temperatures in the range of 600–900 °C (Figure 4a). The as-grown tBLG was scaled up to millimeter with high uniformity in twist angle measured by the LEED pattern (Figure 4b,c). Owing to the steps on SiC substrate as nucleation sites, there was a small portion of few-layer graphene on the quasicrystal tBLG (Figure 4d). The method has merits in making high-quality and large-area tBLG with a precise twist angle of 30°, and the size of tBLG is only limited by the area of SiC substrate. Consequently, the researches on the electronic properties of tBLG adopted this method to prepare samples.<sup>[91]</sup> Excluding the sacrificial layer of *h*-BN, the control over twist angle will be weakened. The tBLG with other twist angle of 4.5° can be obtained, and the uniformity in twist angle also decreased to some extent.<sup>[31]</sup> Exploiting epitaxial growth on SiC, the grain size of tBLG is enlarged to millimeter scale with clean interface, but the control over twist angle suffers from the small range of variation. The tunable twist angle for tBLG with centimeter scale epitaxially grown on SiC has a great prospect.

### 3.3. Stacking Monolayer Graphene

In addition to the direct growth methods described above, the preparation of tBLG is also realized by manual assembly (stacking and folding of monolayer graphene). The operation of stacking involves one monolayer graphene placed vertically on the surface of another monolayer graphene through the transfer process. Previously, the stacking of two graphene layers is a simple overlap through transfer process, resulting in randomly rotational orientation for tBLG. For example, Kim et al. adopted the monolayer polycrystalline CVD-grown graphene as starting materials.<sup>[92]</sup> The continuous transfer of monolayer graphene led to the formation of tBLG with twist angles of 3, 7, 10, 14, 20, and 27°. Although the variable range of twist angle is large, there is no way to precisely control the twist angle at a certain value. The uncertainty originates from the lack of positioning system during the transfer process. Therefore, how to control the twist angle during the stacking process has aroused extensive attention. The use of alignment transfer

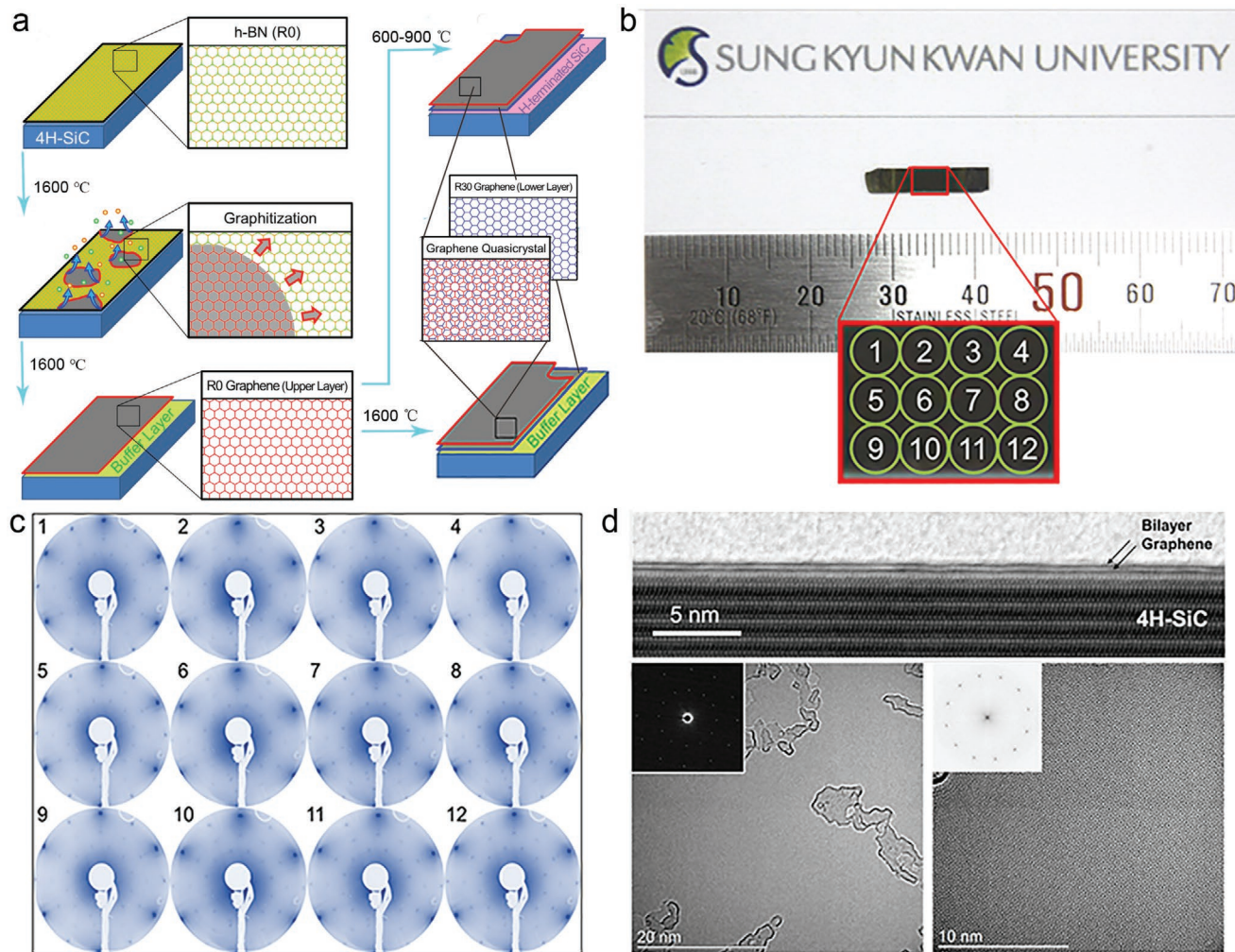


**Figure 4.** The epitaxial growth of tBLG on SiC surface. a) Schematic illustration of epitaxial growth of  $30^\circ$ -tBLG under the guideline of *h*-BN as a sacrificial layer on SiC surface. b) Optical image of large-area tBLG marked with number in different regions. c) The LEED patterns at different positions in sample (b). d) The high-resolution TEM image of tBLG. Top: A cross-sectional image to show the bilayer graphene. Bottom left: few layers of graphene in tBLG. Inset is the SAED pattern. Bottom right: a magnified image with atomic scale. Inset is the Fourier-transformed image. a-d) Reproduced with permission.<sup>[89]</sup> Copyright 2018, American Association for the Advancement of Science.

system is an efficient method to control twist angle, which is similar to the assembly of van der Waals heterostructures.<sup>[93–95]</sup> The basic units of typical alignment transfer machine contain an optical microscope and two positioners as upper and lower sample stages, respectively (Figure 5a). The lower positioner is used to load the bottom graphene and accepts the top graphene. Another positioner is the transfer holder to carry and place the top graphene (Figure 5b). These positioners can be moved along the  $x$ -,  $y$ -,  $z$ -axis directions, and are rotated or tilted by manual adjustment in turn to control the twist angle. Besides, the alignment transfer machine is installed inside or outside a glovebox (Figure 5c). The lower concentration of water and oxygen in glovebox is beneficial to reduce the interlayer adsorbates.

The starting monolayer graphene can be obtained by CVD or mechanical exfoliation. The exfoliated graphene is the popular selection because the transfer procedure leads to the degradation of quality for CVD grown-graphene.<sup>[96,97]</sup> Meanwhile,

the integration of high-quality and low cost for exfoliation method is another attractive factor.<sup>[98]</sup> However, the exfoliated graphene has an irregular shape with rough edges, which is not good for the rotation and alignment. To tackle the issue, the use of reference frame is the basic strategy, including the collimated graphene edges or metal masks. For instance, Tian group developed the femtosecond laser to fabricate straight graphene edges in favor of forming tBLG by alignment transfer system.<sup>[99]</sup> The preparation process was divided into four parts: 1) A femtosecond laser was used to cut single-crystal graphene film for generating the sharp and parallel edges (Figure 5d); 2) a poly (methyl methacrylate) (PMMA) layer was coated on the clipped graphene, and then was tailored along the former cutting lines; 3) one part of graphene film was transferred to a new  $\text{SiO}_2/\text{Si}$  substrate and affixed on the lower positioner, while, another was adhered on the upper positioner which is a glass slide with a hole; 4) two graphene flakes were precisely stacked by alignment transfer machine, and then removed the

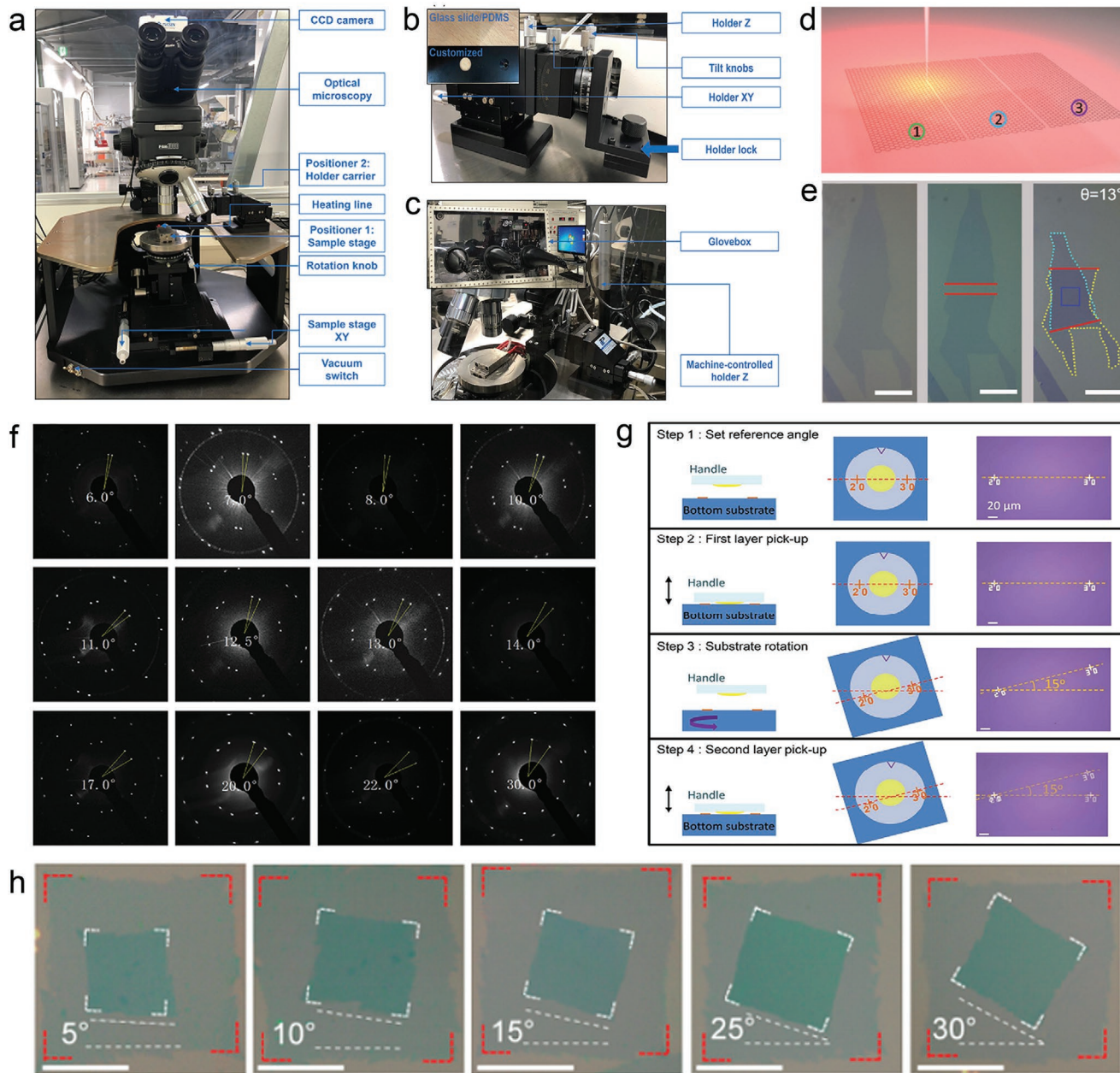


**Figure 5.** The fabrication of tBLG via stacking monolayer graphene. a) Photograph of typical alignment transfer machine. b) The upper micro-positioners as transfer holder to fix top graphene. Inset is a typical structure of top micro-positioners. c) The alignment transfer machine installed inside the glovebox. a–c) Reproduced with permission.<sup>[93]</sup> Copyright 2020, IOP Publishing. d) Schematic illustration of straight and parallel edges of graphene fabricated by femtosecond laser. e) The fabrication process of tBLG under the concept of cutting-rotation-stacking. Scale bar is 50  $\mu\text{m}$ . f) SAED images of tBLG with twist angles from 6 to 30°. d–f) Reproduced with permission.<sup>[99]</sup> Copyright 2016, Wiley-VCH. g) Schematic illustration of the fabrication process of tBLG with metal alignment marks as reference. Reproduced with permission.<sup>[100]</sup> Copyright 2016, American Chemical Society. h) Optical image of large-domain tBLG by layer-by-layer transfer skill. Scale bar is 100  $\mu\text{m}$ . Reproduced with permission.<sup>[103]</sup> Copyright 2016, American Chemical Society.

PMMA for the formation of tBLG (Figure 5e). In the rotation process, the parallel cutting lines play a crucial role for the control over twist angle because it acts as a reference frame. The twist angle of tBLG prepared by this cutting-rotation-stacking method has a wide variation range and a slight deviation of less than 0.1° from the designated one (Figure 5f). Apart from the straight edges of graphene, the metallic alignment marks on substrate also provide accurate references without limits on the

shape and edges of graphene sheets.<sup>[100]</sup> The process flow was as follows: 1) two metallic marks were brought in marking the initial position of graphene film on SiO<sub>2</sub>/Si substrates; 2) the poly(vinyl alcohol)-coated epoxy with *h*-BN as hemispherical handle was used to contact with a portion of monolayer graphene film for the first pick-up; 3) the bottom substrate was rotated with a desired angle and the transfer handle remained stationary; as an example, the twist angle of 1° was obtained by

rotating the right-most alignment mark away from the initial position about 2.5 μm when the distance between two masks was 200 μm; 4) the handle contacted with the remaining portion of graphene film for second pick-up to accomplish the assembly of tBLG (Figure 5g). It is worth noting that two graphene sheets are different regions of the same graphene film to ensure the highly uniform lattice structure of tBLG. Meanwhile, graphene and original substrate can also be detached by the intercalation of water or ethanol, enabling a high-quality interface for tBLG.<sup>[101,102]</sup>

In stacking procedure, the inevitable part is organic polymer that assists the transfer of graphene, and its residual gives rise to the interfacial contaminants. Therefore, a new transfer technique is critical to obtain a clean interface. Liu et al. reported a layer-by-layer transfer skill to fabricate large-domain tBLG with controllable twist angles, avoiding the introduction of polymer contamination in the interlayer.<sup>[103]</sup> The pivotal step was that the PMMA/graphene film was directly stacked onto another graphene/Cu foil by an alignment transfer system. The single-crystalline graphene prepared by CVD had a square shape with straight edges in favor of the rotational alignment during transfer process (Figure 5h). Finally, the PMMA/tBLG was detached from the copper substrate onto the target substrate. The direct contact between graphene layers helps to avoid the interlayer contamination, which is first used in stacking multi-layer graphene as transparent conductive electrode.<sup>[104]</sup> To leave tBLG alone on target substrate, the PMMA was removed by immersing in acetone. Furthermore, there were the additional treatments to improve the removal of polymer in recent years, including the decomposition by annealing in CVD chamber at high temperatures,<sup>[105]</sup> the dissolution with acetic acid,<sup>[106]</sup> and the irradiation with a UV/O<sub>3</sub> lamp.<sup>[107]</sup> Meanwhile, using a strong van der Waals bonding to pick up graphene can avoid the residual of polymer in the interface. Sharpe et al. demonstrated that tBLG encapsulated in two *h*-BN layers displayed ferromagnetic state via the enhanced interactions.<sup>[108]</sup> The *h*-BN, a single atomic layered insulating material,<sup>[109]</sup> provides a great interface contact and strong van der Waals attractions to pick up graphene. A poly(bisphenol A carbonate) film/gel (Gel-Pak DGL-17-X8) tape was used to first pick-up the *h*-BN flake as a substrate. Then, the *h*-BN was aligned partially with an exfoliated monolayer graphene to tear and pick up a portion. Subsequently, the overlap of two graphene layers was precisely controlled under supervision of alignment transfer machine. Finally, stacking another *h*-BN served as packaging layer in surface. Evidently, there is no direct contact between graphene and polymer, accomplishing the purpose of clean interface between graphene layers. Moreover, Imamura et al. prepared tBLG with clean interface/surface by the face to face stacking monolayer graphene/substrate without assistance of transfer medium.<sup>[110]</sup> The twist angle was regulated under the guidance of reflection high-energy electron diffraction with error of ±4°. The successful implementation of this technology was based on the synthesis of easy-to-exfoliate monolayer graphene on SiC surface by adding oxygen. Meanwhile a high vacuum environment was used to promote the stable bonding for tBLG.

Although the stacking process is complex and has low yield, the variability and fine control over twist angle impels this approach to become mainstream in condensed matter

physics. Especially, the encapsulation of tBLG with *h*-BN during stacking process not only isolates the direct contact between polymer and graphene, but also provides an atomically smooth substrate for the characterization of exotic physical properties. Table 1 briefly summarizes the qualitative comparison for the above discussed methods. Moreover, Liu et al. confirmed that the large-area single crystal graphene grown by CVD as starting materials could enlarge the grain size of tBLG, providing an insight into the mass production of tBLG by stacking method.

### 3.4. Folding Monolayer Graphene

Except for the vertical stacking of two separate graphene layers, the folding of one-layer continuous graphene film can effectively assemble into tBLG. Universally, the folding effect occurs in the process of mechanical exfoliation, and the increase in yield for folded graphene is achieved by using water flushing,<sup>[111]</sup> laser or ion ablation,<sup>[32,112]</sup> and mechanical contact scribing where the tools are from scanning tunneling microscope (STM) or atomic force microscope (AFM) tips.<sup>[113]</sup> Using AFM tips to fold graphene was driven by a constant force from the contact mode (Figure 6a), but a defective edge was first produced by continuous scan along a direction with AFM tip in tapping mode (Figure 6b). This pre-treatment was beneficial to reducing the close contact between graphene and substrate, causing a curled edge. Then, the curled edge was fast scanned in contact mode for being pushed toward the interior of graphene to form folding tBLG (Figure 6c). However, the edge would not be completely folded but partly folded because these were pre-formed defects in edges to cause the graphene cutting.<sup>[114]</sup> Obviously, folding with AFM tips is accompanied by the tearing and deformations for graphene. However, the graphene origami through STM manipulation pioneered by Gao et al. showed the repetitive folding and unfolding of graphene without the appearance of defects.<sup>[115]</sup> Briefly, the STM tip was close to graphene edge by reducing the tunneling resistance, and then moved across graphene along a predestinate direction. During the motion, the tip lifted graphene from edge and dragged a portion of graphene along the moving path of the tip to fold graphene at the desired location (Figure 6d). In addition, a reversed process can be performed to unfold the folded graphene with full recovery of the original status even after multiple origami operations (Figure 6e). More importantly, the twist angle can be determined by the folding direction with an accuracy of 0.1°. On the other hand, the tBLG had a folded 1D tubular edge with the non-contact alignment, which behaved as tBLG/carbon nanotubes heterojunction (Figure 6f). The work achieves the undamaged engineering of graphene in atomic precision for the first time and opens the route of graphene-based quantum machines.

The grain size of tBLG concentrates on a few micron or hundreds of nanometers by applying AFM or STM tips to fold graphene. Ruoff group presented a macroscopically folded graphene via self-folding driven by hydrophobicity.<sup>[116]</sup> The self-folding was conducted on a decorated substrate with the hydrophobic and hydrophilic regions. The whole processes were as follows: 1) A PMMA layer was spin-coated on the graphene/Cu foil surface; 2) the tailored substrate contacted

**Table 1.** The qualitative comparison of different stacking methods fabricating the tBLG in terms of cleanliness and controllability of twist angle.

Alignment tool	Cleaness	Transfer method	Notes	Ref.
None	★★	Wet transfer	Weak controllability over twist angle; twice spin-coating; direct contact with PMMA in surface and interface	[92]
Alignment transfer system (collimated graphene edges as reference)	★★	Wet transfer	Good controllability over twist angle with accuracy of 0.1°; additional operations to form collimated edges; spin-coating; direct contact with PMMA in surface and interface	[99]
Alignment transfer system (metallic marks as reference)	★★★	Dry transfer	Good controllability over twist angle; van der Waals attractions; direct contact with the polymer only for <i>h</i> -BN	[100]
Alignment transfer system (collimated graphene edges as reference)	★★★	Wet transfer	Good controllability over twist angle; one spin-coating; direct contact with PMMA in surface; size of tBLG over 100 μm	[103]
Alignment transfer system (metallic marks as reference)	★★★	Dry transfer	Good controllability over twist angle with accuracy of 0.2°; van der Waals attractions; direct contact with the polymer only for <i>h</i> -BN	[108]
Reflection high-energy electron diffraction	★★★★	Dry transfer	Controllability over twist angle with accuracy of 4°; direct contact of graphene layers; sub-millimeter in size	[110]
No mention	★★★	Dry transfer	Van der Waals attractions; hot transfer; direct contact with the polymer only for <i>h</i> -BN	[123]

with the PMMA/graphene/Cu foil, and then was immersed in aqueous ammonium persulfate to etch away the Cu foil; 3) the self-folding of graphene was achieved by slowly withdrawing PMMA/graphene/tailored substrate from water: a part of PMMA/graphene on the hydrophilic region floated on the water, and then folded over other part of PMMA/graphene adhered on the hydrophobic region during the withdrawal process; 4) the PMMA on both outsides were removed to obtain a folded bilayer graphene (Figure 6g). The folded bilayer graphene with different folding angles corresponded to different twist angles. By establishing the relation between folding angles and twist angles, any defined twist angle could be achieved through folding along a certain direction (Figure 6h,i). Meanwhile, the folded tBLG has a tubular edge which promotes the formation of a new heterojunction, delivering unique electronic states. However, the uniformity of large-area folded tBLG has a slight deviation due to the formation of wrinkles and blisters during the folding process. The folding of monolayer graphene offers a new route for assembling tBLG with clean interface, but the twist angle is limited by the scan direction of tips. The extension of variation in twist angle for tBLG by rotating the sample stage in AFM or STM will be the next opportunity.

During the transfer process, the spontaneous formation of wrinkles and blisters has a passive influence on the intrinsic behavior of tBLG.<sup>[117–119]</sup> To obtain the ultra-flat and highly uniform tBLG, the studies on the avoidance of wrinkles and blisters is rapidly developing. Currently, methods of eliminating wrinkles and blisters are the use of AFM tips to flatten materials<sup>[120,121]</sup> and the low temperature annealing.<sup>[122]</sup> For instance, Cao et al. used the hot-transfer technique for stacking two sets of Bernal-stacked bilayer graphene with close contact.<sup>[123]</sup> The pick-up and release process were executed at a temperature of 100 and 170 °C, respectively, providing a reliable route to remove the blisters.

Because the blisters become more mobile and gather at the edge of graphene flakes at a higher temperature, which is similar to the assembly of high-quality multilayer graphene at a temperature higher than the boiling point of water.<sup>[124]</sup> The presences of these subtleties obscure the pristine properties of tBLG, but present opportunities for the tuning of its physical performances.<sup>[125,126]</sup> For instance, the wrinkles in tBLG bring about the zero-field Landau levels like-quantization and a valley polarization, promoting the realization of high-temperature quantum valley Hall effect.<sup>[127]</sup> Moreover, the buckled structures in monolayer graphene is an alternative structure to inducing flat bands without strict-tuning of twist angle, enabling the presence of correlated insulating and superconducting states.<sup>[128]</sup> The reasonable manipulation of wrinkles and blisters in tBLG offers a credible strategy for creating other superlattice systems to explore the unique physical phenomena.

#### 4. The Establishment of Twist Angle

When tBLG is prepared by the above methods, how to establish the rotation angle between two layers of graphene is consistent with the expected twist angle of lattice structures. There are three common approaches to identify the twist angle: 1) The direct measurement of the rotation angle for two graphene layers by goniometer. In some cases, graphene has smooth, straight edges and uniform atomic arrangement without grain boundaries so that the rotation angle of two graphene layers is projected on the relative position of edges, which can be referred to as the twist angle of lattice structure (Figure 7a). The situation is suited for the tBLG consisted of single-crystal graphene with straight and sharp edges. Usually, CVD technique can realize the growth of tBLG made up of two layers of hexagonal single-crystal graphene with straight

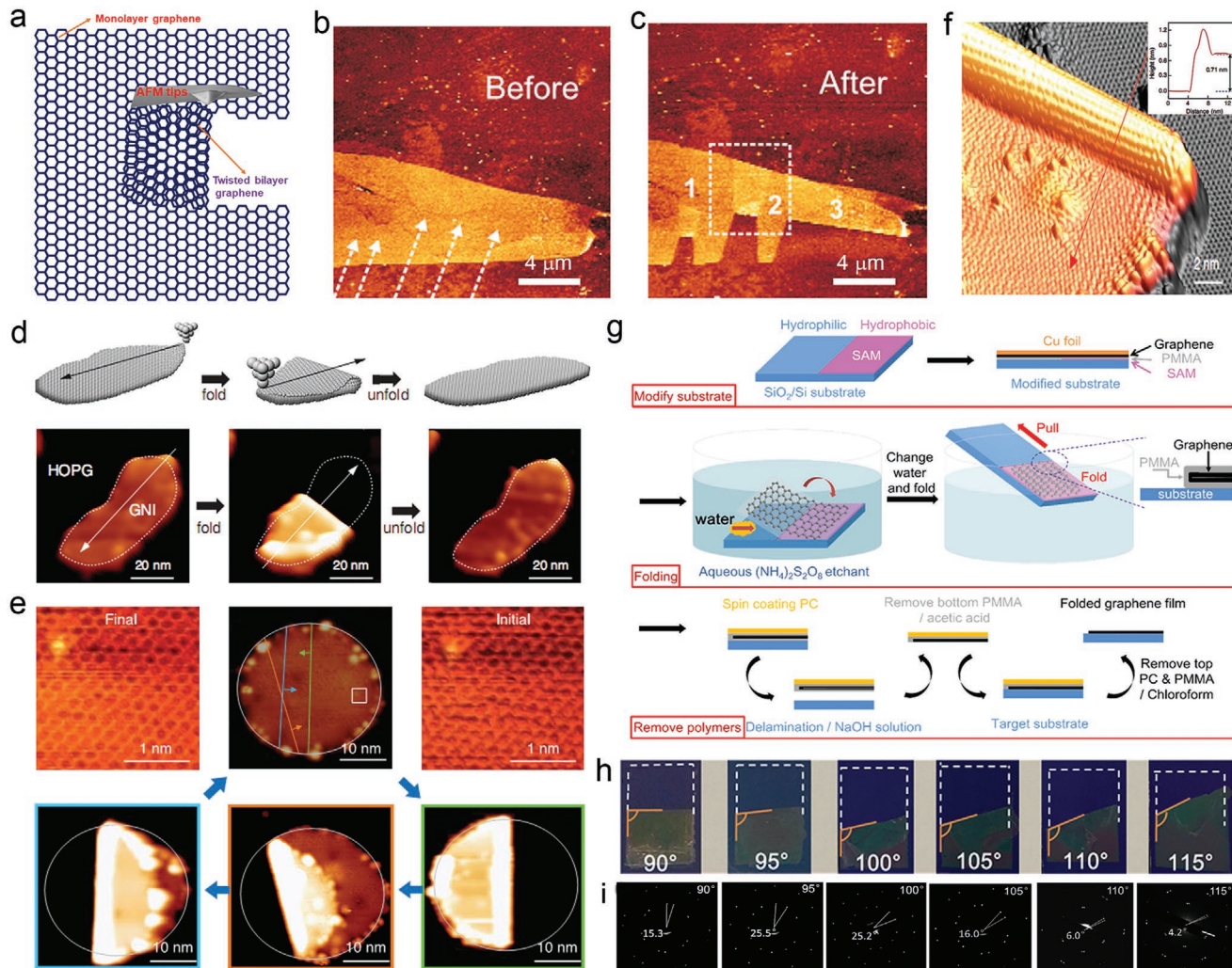


**Figure 6.** The fabrication of tBLG via folding monolayer graphene. a) Schematic illustration of folding graphene via AFM tip. b) The curled edge of graphene prepared by AFM tip in tapping mode. c) The fabricated tBLG by AFM tip in contact mode. b,c) Reproduced with permission.<sup>[114]</sup> Copyright 2013, American Physical Society. d) Schematic (top) and experimental manipulation (bottom) of folding and unfolding a graphene nanoisland (GNI) along arrow direction. e) The lattice structure of graphene after multiple folding and unfolding along different directions. f) 3D STM image of tBLG with 1D tubular edge. Inset is the profile of height, showing the bilayer graphene and tubular edge. d–f) Reproduced with permission.<sup>[115]</sup> Copyright 2019, American Association for the Advancement of Science. g) Schematic illustration of fabricating the macroscopic tBLG from a monolayer graphene film. h) Optical image of folded graphene with different folding angles. i) SAED patterns of folded graphene with different twist angles corresponding to above folding angles. g–i) Reproduced with permission.<sup>[116]</sup> Copyright 2017, American Chemical Society.

edges.<sup>[129]</sup> 2) The diffraction pattern of tBLG to reveal the twist angle. For monolayer graphene, there is only a set of diffraction spots with hexagonal shape. In contrast, the diffraction pattern has 12 spots in bilayer graphene, which can be regarded as a combination of two sets of hexagonal diffraction patterns with a rotation angle. The twist angle is reflected in the rotation of two sets of diffraction spots (Figure 7b).<sup>[44,130]</sup> It should be noted that the AB stacking bilayer graphene with a twist angle of 0° only exhibits a set of diffraction spots similar to the monolayer graphene. Based on this, the LEED (Figure 7c) and selected area electron diffraction (SAED) (Figure 7d) patterns<sup>[131]</sup> can be used to characterize the twist angle, and the establishment of twist angle is not limited by the morphology of tBLG. More importantly, the use of large electron beam with 1 mm × 1 mm in LEED can achieve the characterization of large-area tBLG to

disclose the uniformity, whereas the transfer process may bring a perturbation in SAED patterns. 3) The calculation from the period of Moiré superlattice. The intimate contact and interlayer interaction of two graphene layers produce a Moiré superlattice. The period ( $D$ ) of Moiré pattern is related to the twist angle ( $\theta$ ) and the lattice constant of graphene ( $a$ ), following the equation:

$$D = \frac{a}{2\sin(\theta/2)} \quad (2)$$

Therefore, the twist angle can be mapped by the period of Moiré superlattices.<sup>[132]</sup> Also, the Moiré superlattices can be directly presented in real space by the atomic scale image from TEM (Figure 7e) and STM (Figure 7f). In addition, recent reports demonstrated that a unique R peak of tBLG in Raman

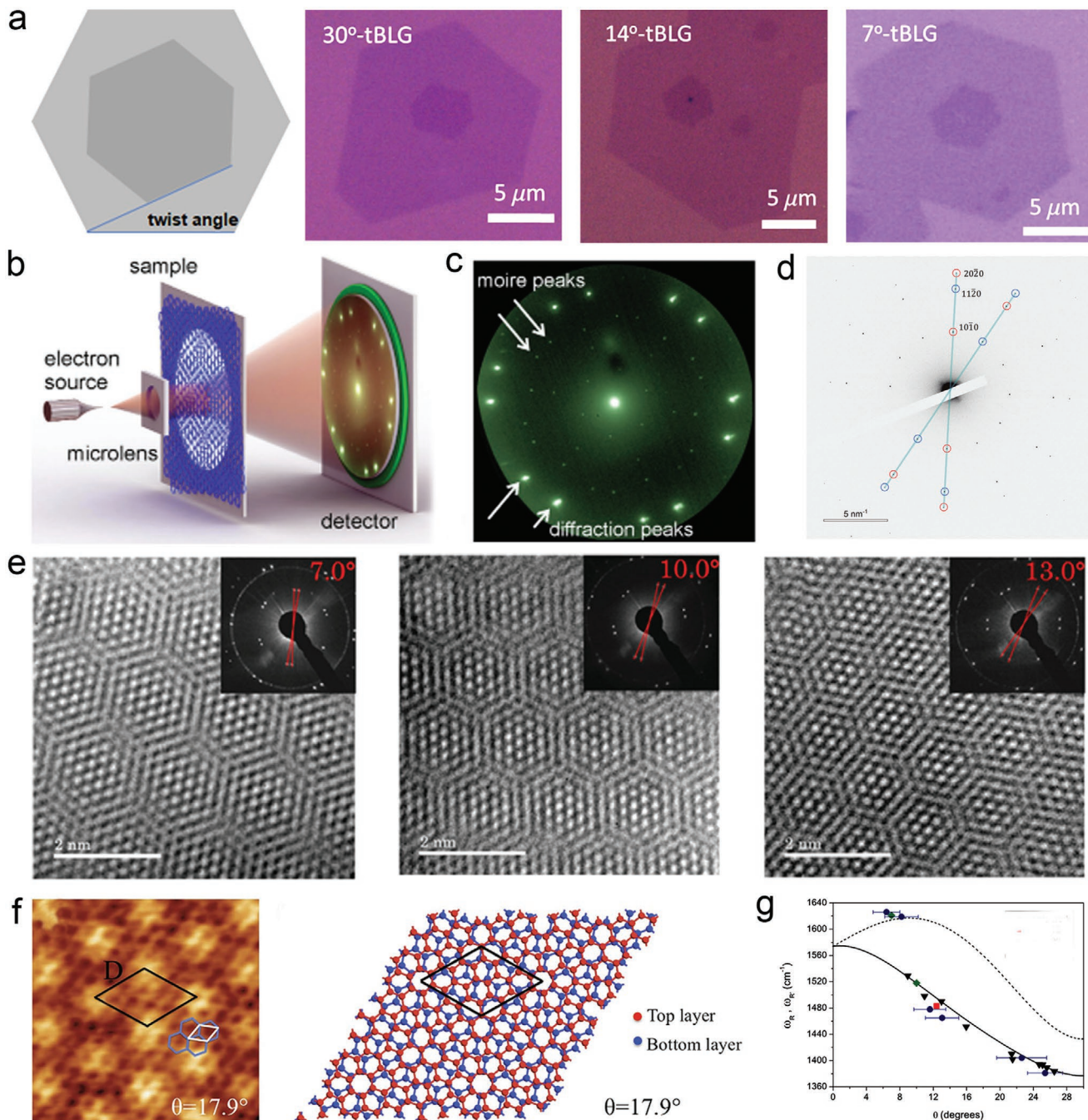


**Figure 7.** The establishment of twist angle by different approaches. a) The establishment of twist angle by measuring the rotation angle between two edges of single-crystal graphene. Reproduced with permission.<sup>[129]</sup> Copyright 2020, Elsevier Ltd. b) Schematic diagram of the emergence of diffraction spots. c,d) LEED patterns. b,c) Reproduced with permission.<sup>[130]</sup> Copyright 2018, Elsevier Ltd. d) SAED patterns. Reproduced with permission.<sup>[131]</sup> Copyright 2020, American Chemical Society. e) Moiré superlattice of tBLG from TEM. Inset is SAED to characterize the twist angle. Reproduced with permission.<sup>[99]</sup> Copyright 2016, Wiley-VCH. f) Left: Moiré patterns from STM (black shows the unit cell); right: its schematic illustration. Reproduced under the terms of the CC-BY 4.0 license.<sup>[132]</sup> Copyright 2016, The Authors, published by Springer Nature. g) R' and R bands frequencies ( $\omega_{R'}$  and  $\omega_R$ ) as a function of the twist angle ( $\theta$ ). Reproduced with permission.<sup>[114]</sup> Copyright 2013, American Physical Society.

spectra originates from the special superlattice-activated intra-valley and intervalley processes. Furthermore, the frequency of R band is interrelated with the twist angle (Figure 7g).<sup>[114,133,134]</sup> From the position of R band, the twist angle of tBLG can be confirmed. Another important information in Raman spectra

is the enhancement of G band intensity for tBLG. When the energy of incident laser is chosen, the maximum enhancement of G band occurs at a specific twist angle. However, the twist angle deduced from Raman spectra is not as direct as the above methods and need the support of huge databases.

## 5. Unique Properties of tBLG and Corresponding Applications

The relative rotation between the upper and lower layers of graphene introduces a twist angle, being restricted into the range of 0° to 30° owing to the six-fold symmetry. The variable twist angle of tBLG leads to the rich physical properties. For example, when twist angle is in the range of 0° to 5°, the strong interlayer coupling results in sharp changes for electronic band structures. The band structures near the charge neutrality point become flat, further leading to the Mott insulating state, unconventional superconducting state,<sup>[135]</sup> and ferromagnetic state.<sup>[136]</sup> When the twist angle increases up to 5°, the band hybridization away from the Dirac point induces the formation of VHS, bringing about the enhanced light absorption. Furthermore, twist angle increases to the maximum value of 30°, the conductivity is higher than that of monolayer graphene or Bernal-stacked bilayer graphene under the condition of interlayer decoupling.<sup>[72]</sup> Meanwhile, a tunable bandgap can be observed under the condition of interlayer coupling.<sup>[43]</sup>

### 5.1. The Correlated Insulating and Superconducting States

At a small twist angle of less than 5°, the low-energy VHS close to the Fermi energy brings about the emergence of superconducting state. In monolayer graphene, this situation is difficult to achieve by doping and gating.<sup>[137]</sup> However, Cao et al. found that bilayer graphene with twist angle of about 1.1° induced the correlated insulating phase and superconducting phase.<sup>[138]</sup> The special twist angle is called as magic angle. Near the magic angle, the Fermi velocity dropped to zero and the electronic band structure became remarkably flat due to the strong electron interaction. When the flat electronic band was half-filled, a correlated insulator was observed, but a superconductor only occurred at temperature down to 1.7 K (Figure 8a). In addition, the correlated insulating phases and superconducting phases were tuned via the magnetic field: 1) At  $B = 0$  T, a Mott insulating state co-existed with the superconducting state; 2) at  $B = 0.4$  T, only a Mott insulating state was observed and the superconductivity disappeared; 3) at  $B = 8$  T, both the Mott insulating state and the superconducting state disappeared, and the tBLG exhibited metal conductivity (Figure 8b). The work reveals that the strong interlayer coupling introduced by magic angle urges tBLG to become a new system for the study of high-temperature superconductivity. Undeniably, the fabrication of tBLG with fine-tuning of twist angle in 1.1° is difficult. Yankowitz et al. expanded the scope of magic angle up to 1.27° by varying the interlayer spacing with hydrostatic pressure.<sup>[139]</sup> At the ambient pressure, the device based on tBLG with an angle of 1.27° responded with insulating states at Moiré unit cell  $\pm ns$  (strongly),  $\pm ns/2$ , and  $+3ns/4$  (weakly). There was no evidence to suggest the presence of superconductivity (Figure 8c). However, applying hydrostatic pressure of 2.21 GPa to this device, the insulating phases was strengthened at corresponding Moiré unit cells, and the resistance rapidly fell to the experimental noise level of about 10 ohms to induce the superconductivity (Figure 8d,e). Meanwhile, the highest critical temperature was elevated up to 3 K due to the reduced Moiré

wavelength at a larger twist angle. Besides, tBLG contacted with a monolayer WSe<sub>2</sub> in favor of the presence of superconductivity even though the twist angle away from the magic angle. When the twist angle of 0.79°, the tBLG displayed metallic behavior over the entire range of electron density, meanwhile the superconductivity was still observed and did not change into an insulator.<sup>[140]</sup> Applying external forces in tBLG can release the restriction of magic angle and increase the critical temperature, which offer an inspiration to broaden the treatment of tBLG. Similarly, a pair of Bernal stacked bilayer graphenes with twist angle is another extension to obtain flat energy band. The standard structure is a four-layer system composed of two AB-stacked graphene bilayers rotated with respect to each other by a small angle (Figure 8f). Twisted double bilayer graphene has a lower symmetry to create a pronounced flat electronic band (Figure 8g). Zhang group tested the device based on the twisted double bilayer graphene with angles of ranging from 0.98 to 1.33° for disclosing the expansion of magic angle.<sup>[141]</sup> The correlated insulating behavior was observed in sample with the twist angle up to 1.33° at displacement fields of  $-0.4$  V nm<sup>-1</sup>, and test temperature high to 15 K. However, the four-probe resistivity of the 1.33°-sample presented abruptly decline at a temperature of about 12 K and saturated at 400 Ω (Figure 8h). The resistivity cannot satisfy the standard of superconductivity because of the non-uniformity of twist angle: In the 1.33°-sample, there are a majority of twist angle of 1.33° and a minority of twist angle of 1.1°. By contrast, a zero resistance for superconducting state was observed when the twist angle changed to 1.28°. The work discloses the important role of low symmetry in the twist system and provides an appropriate route for the expansion of magic angle degree of freedom to induce the exotic quantum states. However, there was a debate that some references claimed that there were no magic angles to induce natural and flat band in twisted double bilayer graphene unless applying external electric fields.<sup>[142,143]</sup> Haddadi et al. solved the debate through band structure calculations.<sup>[144]</sup> A negligence of lattice relaxation effects and the overestimation of trigonal warping effects are the main reasons for the above viewpoint. The intrinsic symmetric polarization introduced into calculations proclaimed that the flat band was a fundamental feature of twisted double bilayer graphene with a magic angle of 1.3° due to the lattice relaxation effects. The use of electric fields provided a further control over the bandwidth and flat-band structure. Apart from twisted graphene, a Moiré superlattice consisting of ABC-trilayer graphene (TLG) and *h*-BN also exhibited the tunable superconductivity under a vertical displacement field due to the strong asymmetry between holes and electrons (Figure 8i).<sup>[145]</sup> At a small displacement field, the system exhibited a metallic phase. When the displacement field was positive, superconductivity never appeared but a correlated Mott insulating state was observed at a temperature below to 20 K at one-quarter and one-half fillings. As the displacement field decreased to  $-0.54$  V nm<sup>-1</sup>, two apparent superconducting domes emerged at low temperatures near the 1/4-filling Mott state (Figure 8j). The appearance of flat bands at tBLG with a small twist angle is a fundamental condition for the correlated insulating and superconducting phases. Moreover, applying external force or changing graphene structure to strengthen the asymmetry can reduce the strict restriction of magic angle and realize high temperature superconductivity.

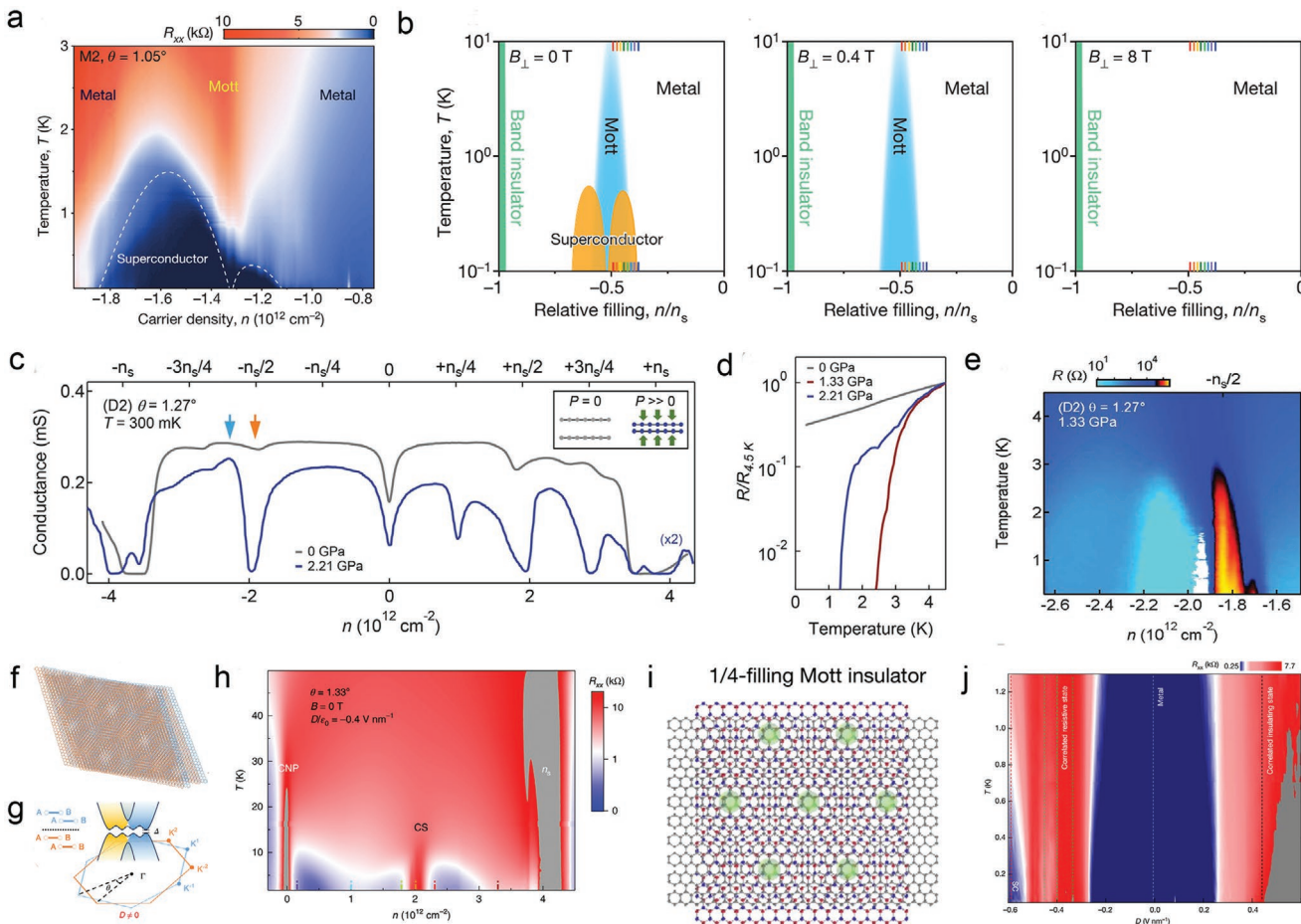


**Figure 8.** The correlated insulating and superconducting states in tBLG. a) Phase diagram of tBLG with twist angle of  $1.1^\circ$  over carrier density and temperature. b) The tunable superconducting phases under different magnetic fields. a,b) Reproduced with permission.<sup>[138]</sup> Copyright 2018, Springer Nature. c) The profile of conductance as a function of carrier density at different pressures. d) The profile of resistance as a function of the temperature at different pressures. e) Phase diagram of tBLG with twist angle of  $1.27^\circ$  over carrier density and temperature. c–e) Reproduced with permission.<sup>[139]</sup> Copyright 2019, American Association for the Advancement of Science. f) Schematic illustration of twisted double bilayer graphene with moiré unit cell. g) Schematic illustration of electronic band structure of twisted double bilayer graphene applied with displacement fields (D). h) Four-probe resistance as a function of temperature and carrier density in twisted double bilayer graphene with an angle of  $1.33^\circ$  when  $D/\epsilon_0 = -0.4 \text{ V nm}^{-1}$ . The correlated insulating states (CSs) are flanked by two low-resistivity domes. f–h) Reproduced with permission.<sup>[141]</sup> Copyright 2020, Springer Nature. i) Schematic illustration of the triangular ABC-TLG/h-BN Moiré superlattice and the 1/4-filling Mott insulating state. j) Tunable electronic phases with the displacement field (D). i,j) Reproduced with permission.<sup>[145]</sup> Copyright 2019, Springer Nature.

## 5.2. Ferromagnetic State

At a small twist angle, the appearance of flat superlattice minibands induces not only the correlated insulating states and superconducting states but also ferromagnetic states for tBLG. Sharpe et al. showed the clear experimental evidence about ferromagnetism in  $1.17^\circ$ -tBLG by measuring magnetotransport.<sup>[108]</sup> The observation of a large anomalous Hall resistance of  $6 \text{ k}\Omega$  in a narrow range of carrier density near three-quarters filling in conduction band suggested the remaining magnetization in tBLG (Figure 9a). Moreover, in magnetic field of 0, the differential Hall resistance of tBLG followed hysteresis loops when the dc bias was swept between  $\pm 75 \text{ nA}$ . After tBLG was magnetized in a field of  $-500 \text{ mT}$ , the hysteresis loops were repeatable and reversible when the dc bias was ramped from 0 to  $-75 \text{ nA}$ . The switching of differential Hall resistance is similar to other ferromagnetic materials (Figure 9b). Besides, the direction of

the magnetization can be switched by the small current due to the symmetry breaking of tBLG on *h*-BN substrate.<sup>[146]</sup> These phenomena reveal that the appearance of ferromagnetic states is notable in tBLG system without imposing any limits of impurities or defects. It should be noted that ferromagnetism and superconductivity are two typical phases in tBLG with a small twist angle so that there are competing or intertwined orders. Wu et al. took twisted double bilayer graphene as an example to theoretically study the orders of ferromagnetism and superconductivity.<sup>[147]</sup> The ferromagnetism in twisted double bilayer graphene was driven by Coulomb repulsion so that it was stable against spin-magnon excitations. Moreover, the ferromagnetic gap as a function of the layer dependent potential had a dome shape, which explained the appearance of ferromagnetic insulator at the finite range of displacement field (Figure 9c). The stability of ferromagnetic state is limited in the finite bandwidth. Moreover, the quantum geometry of band plays an

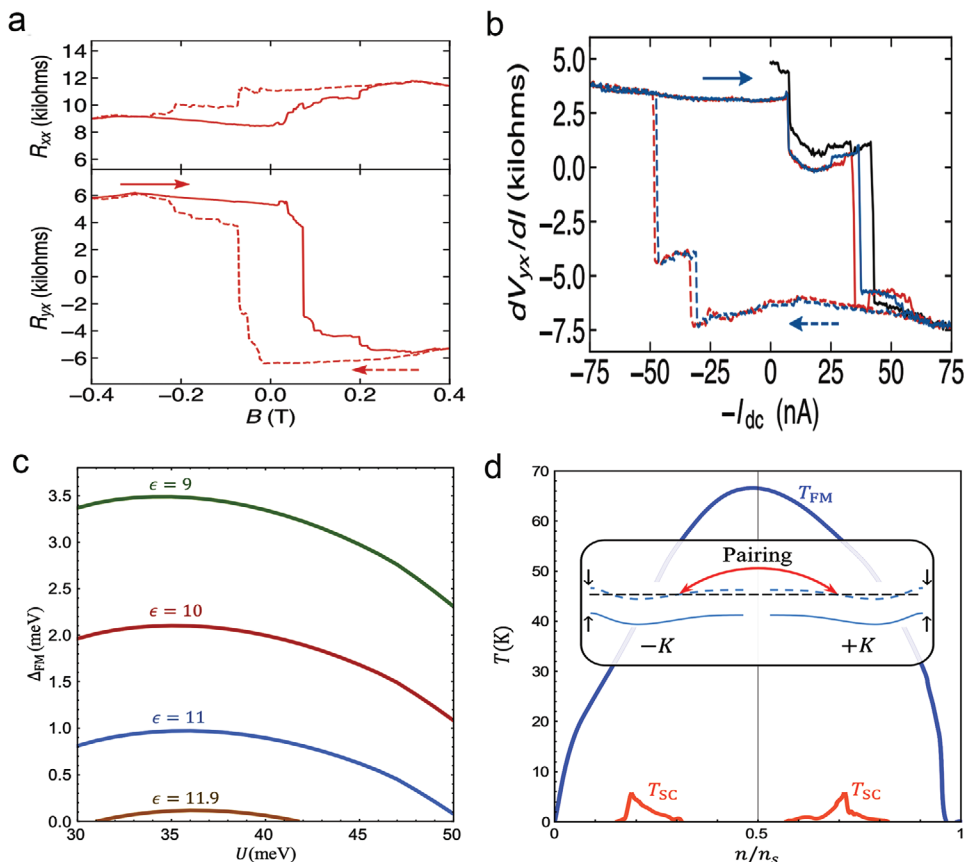


**Figure 9.** The ferromagnetic state in tBLG. a) The profiles of the longitudinal resistance ( $R_{xx}$ , upper panel) and Hall resistance ( $R_{yx}$ , lower panel) as a function of magnetic field ( $B$ ). b) The profiles of the differential Hall resistance ( $dV_{yx}/dI$ ) as a function of the applied dc bias ( $I_{dc}$ ) after magnetizing the sample in a  $-500$  mT field and returning to  $B = 0$ . The black trace is the condition of  $I_{dc}$  from  $0$  to  $-75$  nA. The red and blue traces are the condition of  $I_{dc}$  between  $\pm 75$  nA and opposite sweep directions. a,b) Reproduced with permission.<sup>[108]</sup> Copyright 2019, American Association for the Advancement of Science. c) The profiles of the gap of ferromagnetic insulator ( $\Delta_{FM}$ ) as a function of the layer potential difference ( $U$ ) at different dielectric constants ( $\epsilon$ ). d) The profiles of transition temperatures as a function of the filling factor ( $n/n_s$ ). Blue line is ferromagnetism and red lines are superconductivity. Inset is the schematic illustration of the intervalley pairing in the ferromagnetic state. c,d) Reproduced with permission.<sup>[147]</sup> Copyright 2020 American Physical Society.

important role in enhancing or weakening the ferromagnetism of tBLG.<sup>[148]</sup> For superconductivity, it was unstable due to the modulation by electron-acoustic phonon interactions against with electron-electron for ferromagnetism, while, at half filling, the superconductivity could emerge on both the hole and electron sides of ferromagnetic insulators (Figure 9d). The competition between ferromagnetism and superconductivity is helpful to guide the application tBLG in different fields.

### 5.3. Solitons

In addition, tBLG with a small twist angle can be regarded as a network of graphene domain with AB/BA stacking order due to the reduction of unfavorable AA stacking regions caused by atomic relaxation in strain fields.<sup>[149]</sup> The transition region of AB/BA stacked bilayer graphene is an 1D soliton-like domain wall, which is divided into the tensile (perpendicular to the Burgers vector) and shear (parallel to the Burgers vector) type (Figure 10a,b). The formation of soliton networks in tBLG brings about the essential changes in plasmonic and electronic

properties. Wang et al. found that the plasmon reflection in tBLG exhibited different behaviors at the tensile and shear soliton-like domain wall and could be controlled by electrostatic gating.<sup>[150]</sup> The tensile and shear solitons were characterized by the near-field infrared nanoscopy due to the different infrared responses. In near-field optical images, the tensile and shear solitons were located by double-bright-line and single bright-line, respectively. With the increase of gate voltage, both tensile soliton and shear soliton became stronger, but the tensile soliton was brighter than shear soliton (Figure 10c). The distinct behavior suggested that there is higher plasmon reflectance in tensile soliton. Besides, their group also demonstrated the topologically protected valley transport existed in tBLG with soliton-like domain wall.<sup>[151]</sup> The resistance in tBLG with soliton-like domain wall was much smaller than those in bilayer graphene without soliton (Figure 10d), disclosing the presence of valley-polarized one-dimensional conducting channels in tBLG with soliton-like domain walls. Similarly, the electronic transport behaviors were markedly different across the tensile and shear soliton-like domain wall in tBLG.<sup>[152]</sup> The additional electron scattering at soliton-like domain wall led to an extra voltage

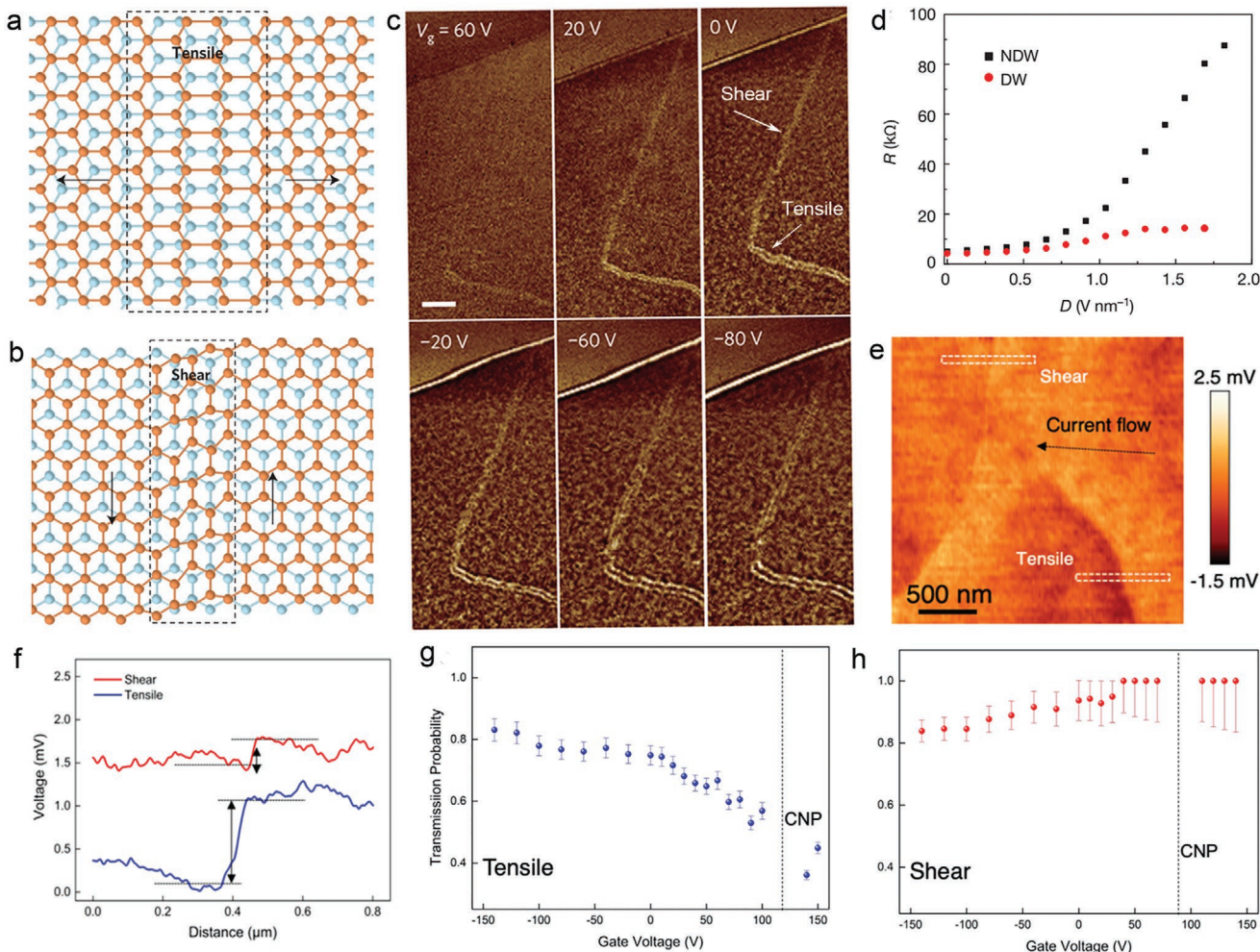


**Figure 10.** The different plasmonic and electronic properties across the soliton-like domain wall. a) The schematic illustrations of tensile soliton-like domain wall. b) The schematic illustrations of shear soliton-like domain wall. c) The shear soliton and tensile soliton in tBLG characterized by near-field infrared nanoscopy and their changes in contrast at different gate voltages. a–c) Reproduced with permission.<sup>[150]</sup> Copyright 2016, Springer Nature. d) The profiles of resistance ( $R$ ) as a function of the displacement field ( $D$ ) for bilayer graphene with soliton-like domain wall (DW, red dot) and without soliton (NDW, black squares). Reproduced with permission.<sup>[151]</sup> Copyright 2015, Springer Nature. e) The voltage mapping of tBLG with soliton-like domain wall (shear and tensile) on  $\text{SiO}_2/\text{Si}$  substrate. f) The profile of voltage drops across the shear and tensile soliton which are displayed in (e). The profile of transmission probability as a function of the gate voltage at g) tensile soliton and h) shear soliton. e–h) Reproduced with permission.<sup>[152]</sup> Copyright 2020, American Chemical Society.

drop from the scanning voltage microscopy, and the drop of voltage at the tensile soliton was much higher than that at the shear soliton (Figure 10e,f). Meanwhile, the electron transmission was unambiguously different at the tensile and shear soliton. The tensile soliton was highly reflective and became more transparent with increase of carrier density by applying negative gate voltage. While the shear soliton maintained the high transmission probability at all gate voltages, even approaching to 1 at the charge neutrality point (Figure 10g,h). Currently, the experimental study of soliton-like domain wall faces great challenges due to the nanostructure with widths of 6 nm for shear soliton and 11 nm for tensile soliton. The physical properties across the soliton-like domain wall are easily covered by those of the bulk graphene. These works have disclosed the visualization of soliton-like domain wall by near-field infrared nanoscopy, and have obtained the real response about

physical properties of the tBLG with solitons. The plasmonic and electronic properties are different across the tensile and shear solitons. Thus, the novel nanoelectronic devices based on such features is a new breakthrough.

#### 5.4. The Enhanced Optical Absorption

When the twist angle is larger than  $5^\circ$ , tBLG has the Moiré superlattice with a shorter period, generating a new electronic phase of VHS in the density of state, and the energy interval of VHS increases monotonously with the twist angle (Figure 11a).<sup>[153]</sup> The emergence of VHS in tBLG leads to the optical absorption higher than monolayer graphene (optical absorption of 2.3%) due to the strong light-matter interaction, reflecting in the phenomena of an improved chemical

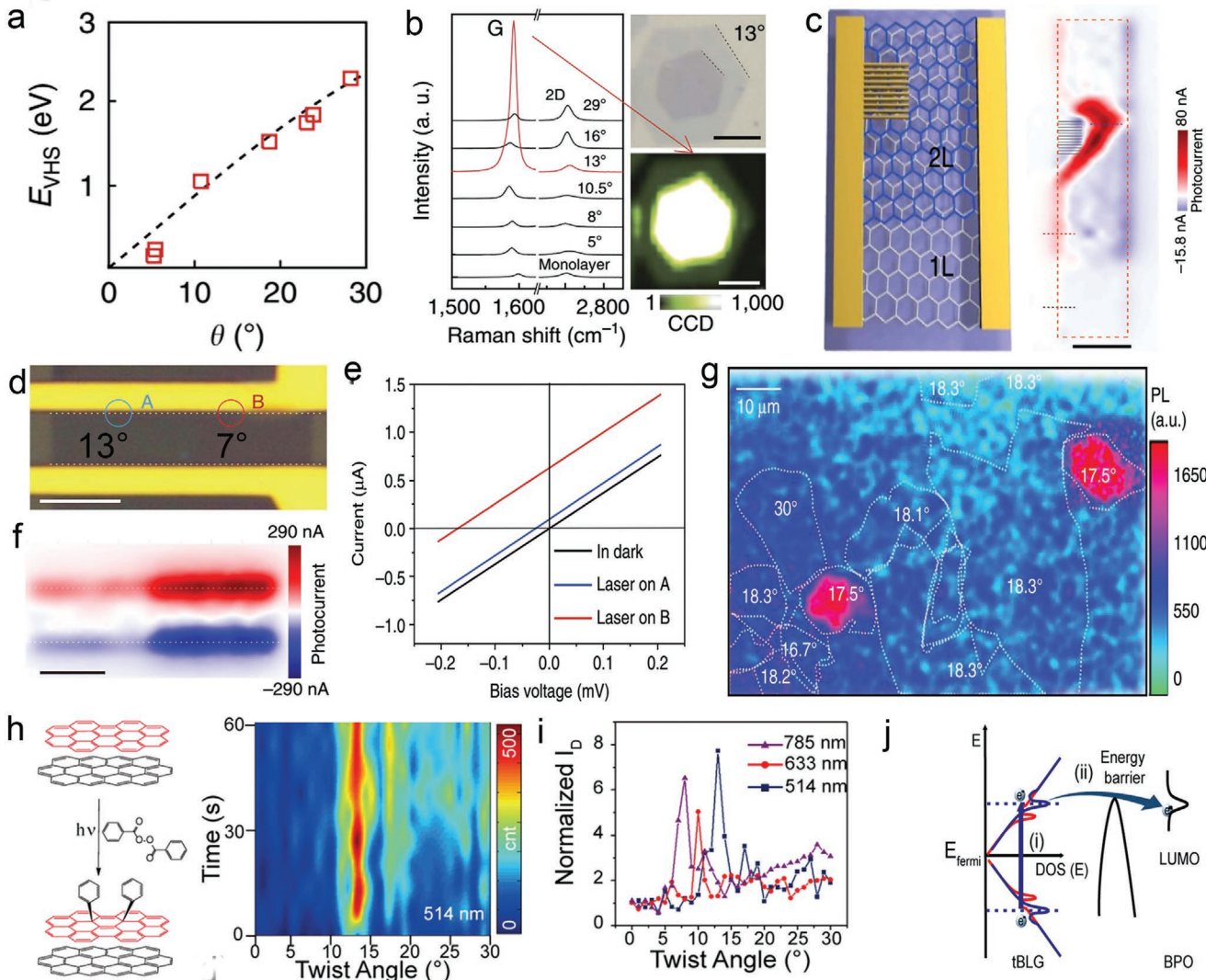


**Figure 11.** The optical application of tBLG. a) The curve of energy interval of VHS as a function of twist angle. b) Left: the Raman spectra of tBLG with different twist angles. Top right: the optical image of 13°-tBLG on  $\text{SiO}_2/\text{Si}$ . Bottom right: the enhanced G-band intensity mapping image of 13°-tBLG. Scale bars are 10  $\mu\text{m}$ . c) Left: schematic illustration of photodetector with monolayer graphene (1L) and tBLG (2L) as channel materials. Right: scanning photocurrent image of the photodetector. d) Optical image of photodetector with twisted graphene (angle of 7° and 13°). Scale bar is 5  $\mu\text{m}$ . e) The current–voltage curves under different conditions. f) Scanning photocurrent images of the device based on tBLG with different twist angles. Scale bar is 5  $\mu\text{m}$ . a–f) Reproduced under the terms of the CC-BY 4.0 license.<sup>[156]</sup> Copyright 2016, The Authors, published by Springer Nature. g) Scanning photoluminescence map of tBLG with different twist angles after two photon excitations. Reproduced under the terms of the CC-BY 4.0 license.<sup>[157]</sup> Copyright 2019, The Authors, published by Springer Nature. h) Left: schematic illustration of the reaction between tBLG and benzoyl peroxide. Right: the evaluation of D band intensity in tBLG as a function of twist angles and reaction time under the irradiation of laser with 514 nm. i) The relationship between the D band intensity and the twist angle (normalized with that of AB-stacked bilayer graphene). j) Hot electron transfer mechanism for the dissociation of benzoyl peroxide (BPO) with assistance of tBLG. h–j) Reproduced with permission.<sup>[158]</sup> Copyright 2015, American Chemical Society.

reactivity and an enhanced intensity of G band in Raman spectra (Figure 11b).<sup>[154,155]</sup> Hence, tBLG with VHS is promising in optical applications. For example, Liu et al. fabricated the tBLG based photodetectors which help to enhance the photocurrent and to reach a wavelength selectivity.<sup>[156]</sup> The scanning photocurrent of tBLG was 10.5 times stronger than that of the monolayer graphene due to the enhanced optical absorption by VHS (Figure 11c). More importantly, the photodetectors based on tBLG with different twist angles had the selective enhancement of photocurrent. The device based on 13°-tBLG generated a much higher photocurrent (0.63 mA) than that of the

device with 7°-tBLG (0.097 mA) measured under the 532-nm laser irradiation (Figure 11d,e). The net photocurrent mapping of two devices displayed similar conclusion that the generation of photocurrent had about 6.6 times disparity (Figure 11f). Besides, the wavelength of incident laser changed from 532 to 638 nm, the maximum enhancement of photocurrent was found in the 10.5°-tBLG. The photocurrent is strengthened selectivity because the energy of incident photon needs to match the energy interval of two VHS in tBLG. The work for the first time realizes the fabrication of optoelectronic devices based on tBLG, showing that the promising optical properties

of tBLG can be translated into practical application. Also, the photoluminescence emission of tBLG was tuned by twist angle after being collected at 2-photon excitation ( $2 \times 1.26$  eV).<sup>[157]</sup> Strikingly, the domains of  $17.5^\circ$ -tBLG showed a five-time enhancement in photoluminescence compared with the neighboring domains of tBLG with other twist angles (Figure 11g). Besides, the appearance of VHS in tBLG also affects its photochemical reactivity that a higher reaction probability is triggered by higher optical absorption. Liu et al. used the chemical reaction between graphene and benzoyl peroxide to discuss the photochemical reactivity of tBLG with different twist angles.<sup>[158]</sup> When 514 nm laser was chosen as the light source,  $13^\circ$ -tBLG exhibited a fastest reaction rate with the highest phenyl group coverage due to the enhanced absorption of incident laser (Figure 11h). Interestingly, the change of laser power led to the shift of twist angle for the optimum photochemical reaction: The twist angles of  $10^\circ$  and  $8^\circ$  had the enhanced reaction rate at lasers of 633 and 785 nm, respectively (Figure 11i). The selective enhancement of chemical reactivity is derived from the transfer of hot electron onto the lowest unoccupied molecular orbital of benzoyl peroxide, which is triggered by the optical absorption of tBLG (Figure 11j). In the above works, the enhanced optical absorption in the visible or near-infrared range is based on the existence of VHS in tBLG with relatively large twist angles, but Deng et al. demonstrated that the mid-infrared photoresponse in tBLG with a small twist angle of  $1.81^\circ$  benefits from the superlattice bandgap.<sup>[159]</sup> The response range of wavelength was from 5 to  $12\text{ }\mu\text{m}$ , and the photoresponsivity reached up to  $26\text{ mA W}^{-1}$  at  $12\text{ }\mu\text{m}$ . These works show that the twist angle of tBLG is a significant parameter in its physical and chemical properties. The enhanced optical absorption drives the possible use of tBLG in photodetector or as a catalyst in photochemical reaction.

### 5.5. Tunable Bandgap

When the twist angle decreases to  $0^\circ$ , the bilayer graphene with AB stacking order has a tunable bandgap under the transverse electrical field. The use of electrical field breaks the symmetry between the top and bottom graphene layers to induce a band gap up to 0.2 eV by theoretical calculation.<sup>[160,161]</sup> In experimental observations, Ruoff group found that CVD grown AB-stacked bilayer graphene with half-millimeter size had great electrical quality with maximum bandgap of 103 meV and high on/off current ratio of  $10^4$  in field-effect transistor (FET).<sup>[162]</sup> If the twist angle increases to less than  $2^\circ$ , the bandgap of tBLG opens at the sub-band edge of triangular superlattice with the value of 20 meV due to the lattice relaxation.<sup>[163]</sup> Further, the bandgap first increases and then decreases with the increase of twist angle (less than  $2^\circ$ ).<sup>[164,165]</sup> In addition, when the twist angle increases to  $30^\circ$  and the strong interlayer coupling still occurs on the tBLG, the band gap opening becomes more obvious at M point of graphene with  $30^\circ$ -orientation ( $M_{30^\circ}$ ) compared with other positions in momentum space (Figure 12a,b). The gap size has the maximum value of  $\approx 280$  meV at the  $M_{30^\circ}$  point and decreases along the distance away from  $M_{30^\circ}$  (Figure 12c).<sup>[43]</sup> Also, the twisted double bilayer graphene with a large twist angle has an intrinsic opened bandgap due to the inequivalent

electrostatic potentials in the external and internal graphene layers.<sup>[166]</sup> The different electrostatics in graphene layers induce the interlayer bias to open up the bandgap, which shares the similar principle with the bandgap opening in AB stacked bilayer graphene by applying different gate voltages.<sup>[167]</sup> It is well known that the ultrahigh carrier mobility allows graphene to become an important candidate for post-silicon electronic devices, but the absence of bandgap is the greatest obstacle for the practical application in FET.<sup>[168,169]</sup> Hence, twisted graphene with a tunable bandgap becomes a powerful candidate for using in FET. A dual-gate FET configuration is a common architecture to characterize the electron transport of tBLG (Figure 12d). If the resistance at the Dirac voltage increases with out-of-plane electric field in both positive and negative directions (Figure 12e,f), it means that tBLG has a tunable energy bandgap which increases with a transverse field. The carrier mobility of tBLG extracted from FET device is in the range of  $672\text{--}1695\text{ cm}^2\text{ V}^{-1}\text{ s}^{-1}$  reported by Liu et al.<sup>[29]</sup> On the other hand, the current ( $I$ )-voltage ( $V$ ) measurements of tBLG executed by conductive AFM could also convey the information of bandgap and carrier mobility.<sup>[170]</sup> The nonlinear characteristics of the  $I/V$  curve suggested the semiconducting behavior of tBLG compared to other kinds of graphene (Figure 12g). Moreover, the transport gap was obtained from the curve of  $dI/dV$  versus  $V$ , where the width of the  $\Delta V = 0$  region was transport gap of about 0.5 V (Figure 12h). The profiles of mobility as function of temperature at different carrier concentrations showed a maximum mobility of  $2050\text{ cm}^2\text{ V}^{-1}\text{ s}^{-1}$  (Figure 12i). The tunable bandgap renders tBLG to be promising in FETs, thereby showing the potential prospects in logical circuits.

### 5.6. Lithium Intercalation and Diffusion

Apart from the electrical, optical, and magnetic properties, the introduction of lithium atom into tBLG also shows interesting phenomena. It is difficult for intrinsic graphene sheet to have great performance in lithium ion batteries due to the negligible mass and the inadmissibility of absorbing lithium atoms,<sup>[171,172]</sup> but lithium ion can intercalate and diffuse in bilayer graphene along the interface rather than the top or bottom layer. Moreover, the lithium diffusion rate in bilayer graphene is faster than those in monolayer graphene.<sup>[173]</sup> However, the intercalation of lithium into tBLG has not been systematically understood. Larson et al. reported the effects of lithium intercalation in tBLG using the first-principle calculations.<sup>[174]</sup> The intercalation of lithium atom have priority in the highly localized AA regions of tBLG, and the intercalation energy of a single lithium atom increases with the distance away from the center of the AA region (Figure 13a). When the twist angle is small, the relative size of the AA region increases with the twist angle, implying the more intercalation of lithium atom. On the other hand, lithium intercalants are sensitive not only to the carbon atomic arrangement in tBLG, but also to the presence of other nearby lithium atoms (Figure 13b). The intercalation energy first decreases and increases with the distance between lithium atoms. In turn, the intercalation of lithium into tBLG has an influence on the band structure to tune its Moiré physics: 1) The average layer spacing of bilayer graphene increases with

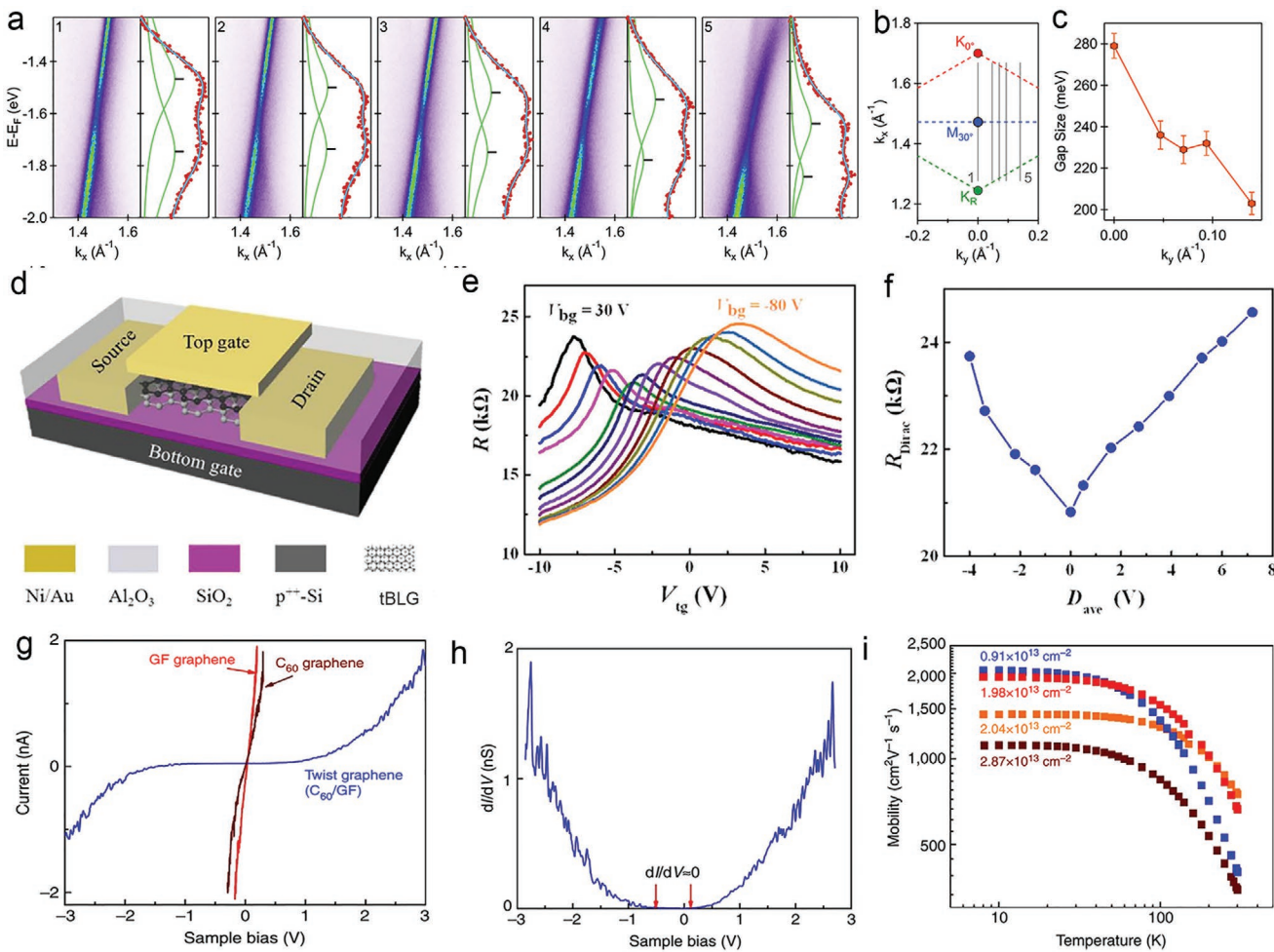


**Figure 12.** The electrical transport of tBLG. a) The bandgap opening at different positions in the  $k$  space shown in (b). b) Schematic BZ showing the different positions in (a). c) The bandgap size as a function of the  $k_y$  direction. a–c) Reproduced with permission.<sup>[43]</sup> Copyright 2018, National Academy of Sciences. d) Schematic illustration of the dual-gate FET devices based on tBLG as channel material. e) The profiles of resistivity as a function of top-gate voltage ( $V_{tg}$ ) at different bottom-gate dielectrics ( $V_{bg}$ ). f) The profiles of resistance at the Dirac voltage ( $R_{\text{Dirac}}$ ) as a function of the average displacement field ( $D_{\text{ave}}$ ). d–f) Reproduced under the terms of the CC-BY 4.0 license.<sup>[29]</sup> Copyright 2015, The Authors, published by Springer Nature. g) The profiles of  $I/V$  with different samples. CF graphene was obtained by the thermal decomposition on SiC substrate with graphite filament as carbon source. C<sub>60</sub> graphene was obtained by C<sub>60</sub> as carbon source. h) The profile of  $dI/dV$  versus  $V$  for twisted graphene. i) The profiles of mobility as function of temperature at different carrier concentrations. g–i) Reproduced with permission.<sup>[170]</sup> Copyright 2015, Springer Nature.

the intercalation of lithium, and is the largest at AB region (Figure 13c). Consequently, the interlayer interaction become weak; 2) the intercalation of lithium makes electronic states and Fermi level adjustable at much larger twist angles (Figure 13d). The work discloses the lithium intercalation in tBLG, guiding the development of graphene materials in lithium ion batteries.

## 6. Conclusion and Prospects

The research on tBLG is developing with a fast speed, and the disclosure on the relationship between the structural features, manufacturing techniques, and physicochemical properties is instrumental in promoting the use of tBLG into market. Recently, many efforts have been devoted to understanding the unique physical and quantum properties of tBLG caused by the reconstruction of lattice structure, but the progress in fabrication

and application remains slow. The preparation methods have typically made a compromise between the precise control over twist angles and the super-clean interface, which directly affects the physical properties and application of tBLG. Using alignment transfer machine to stack monolayer graphene can reach the goal of variability and controllability for twist angle, but the use of organic polymers in transfer process inevitably brings the residual pollutants in the interface or the topmost layer of tBLG. Another biggest bottleneck is the low yield: tBLG is formed one by one after multiple complicated operations, which cannot achieve the mass production by primary operation process. Thus, the stacking monolayer graphene method is suitable for the research on basic physical properties of tBLG. Similarly, the method of folding monolayer graphene by AFM or STM tips has the low yield for the preparation of tBLG. Differently, the interface pollution problem can be solved by selecting mechanically exfoliated graphene instead of CVD-grown graphene as

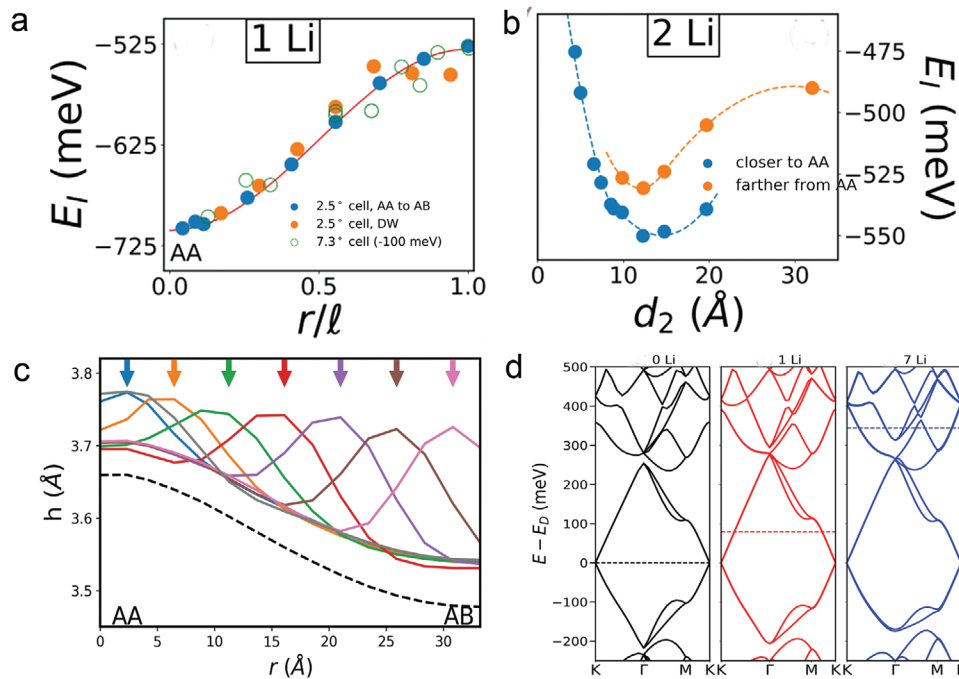


**Figure 13.** The intercalation of lithium atom into tBLG. a) The profile of intercalation energy for a single Li atom as a function of  $r/l$ , where  $r$  is the distance from the center of the AA region and  $l$  is the distance between the center of AA region and the neighboring AB (or BA) region. b) The profile of intercalation energy for a pair of Li atoms as a function of the distance between the Li atoms ( $d_2$ ). c) Average separation ( $h$ ) between graphene layers along a line from AA to AB regions. Colored curves show the separation with a Li intercalant, marked with colored arrows. The dashed black curve shows the layer separation at empty bilayer graphene. d) The band structures of the 2.45°-tBLG with the intercalant of 0, 1, and 7 Li atoms in the AA region. A dashed line is the Fermi level. a-d) Reproduced with permission.<sup>[174]</sup> Copyright 2020, American Physical Society.

starting material. However, the folding orientation is hard to manipulate, which is decided by the scan direction of AFM or STM tips. The domain of tBLG prepared by manual assembly is only a few microns, even nanometers in size, but the twist angle is uniform when the wrinkles and blisters are excluded during assembly process. For the direct growth of tBLG, CVD or epitaxial growth on SiC tends to synthesize the large-area tBLG, which can be regarded as the realization of mass production relative to the stacking or folding technology. The major problems are the limited variable range of twist angle and the uniformity of twisted region. The growth of tBLG on substrate is in the near equilibrium state, leading to the twist angle concentrated at 0 and 30° due to the lower interface energy. Therefore, it is difficult to grow tBLG with other twist angles owing to the requirements of extra energy to break the balance. In addition, there are different twisted domain in large-area tBLG due to the existence of grain boundary for graphene layers, but the direct growth of tBLG consisting of two layers of hexagonal single crystal graphene can avoid this problem. It is well known that the expression of physical performance is related to the quality of tBLG, including twist angle, uniformity, and interface cleanliness. Thus, the improvement of preparation methods is the future development trend. In particular, the direct growth of high-quality and super-clean tBLG with various twist angles has great practical significance.

The study on the application of tBLG has relatively a narrow scope compared to that of untwisted graphene. Owing to the different twist angle, tBLG shows the different physical properties in turn to use in diverse fields. For example, tBLG with

small twist angle has great performance in superconductivity, magnetism and lithium intercalation, and diffusion, endowing potential prospect in spin device, magnetic memories with low energy dissipation, and energy storage and conversion. Therefore, the manual assembly (stacking or folding monolayer graphene) is the most suitable methods. Because the use of alignment transfer machine provides a guarantee for the formation of small twist angle. Meanwhile, tBLG with large twist angle (10°–30°) have the tunable bandgap and VHS, which promote the application in the electrical and optical application, including FET, photodetector, and photochemical reaction. Also, the other electronic switching devices or optical sensor will be promising when tBLG with large twist angle is used as active materials. Owing to the restriction of growth substrate, the 0°- and 30°-stacking orientations for tBLG are dominant architecture in CVD process, and other twist angles of 10°–20° are occasionally observed. Thus, the applications of CVD-grown tBLG focus on these electrical and optical devices, and so does tBLG epitaxially grown on SiC. The weak controllability of twist angle for CVD technique hinders the broad application of tBLG in superconductivity and magnetic memories. The diversity of twist angles plays an important role to extend the application of CVD-grown tBLG. Besides, the improvement of uniformity in twist angle is another essential for the practical usage. In summary, the new electronic state of tBLG caused by the interface coupling gives rise to a series of exotic physical phenomena which are not found in monolayer graphene. The twisted effect is expected to develop in other 2D materials to find other attractive physical properties and applications.

## Acknowledgements

The authors are grateful for the financial support from the Strategic Priority Research Program of the Chinese Academy of Sciences (XDB30000000) and the National Natural Science Foundation of China (61390502).

## Conflict of Interest

The authors declare no conflict of interest.

## Keywords

ferromagnetic state, folding monolayer graphene, Moiré superlattice, topological physical properties, twisted bilayer graphene

Received: July 21, 2020

Revised: October 9, 2020

Published online: February 22, 2021

- [1] L. Lin, J. Zhang, H. Su, J. Li, L. Sun, Z. Wang, F. Xu, C. Liu, S. Lopatin, Y. Zhu, K. Jia, S. Chen, D. Rui, J. Sun, R. Xue, P. Gao, N. Kang, Y. Han, H. Q. Xu, Y. Cao, K. S. Novoselov, Z. Tian, B. Ren, H. Peng, Z. Liu, *Nat. Commun.* **2019**, *10*, 1912.
- [2] S. Rathi, I. Lee, D. Lim, J. Wang, Y. Ochiai, N. Aoki, K. Watanabe, T. Taniguchi, G. H. Lee, Y. J. Yu, P. Kim, G. H. Kim, *Nano Lett.* **2015**, *15*, 5017.
- [3] C. Lee, X. Wei, J. W. Kysar, J. Hone, *Science* **2008**, *321*, 385.
- [4] X. Xu, D. Yi, Z. Wang, J. Yu, Z. Zhang, R. Qiao, Z. Sun, Z. Hu, P. Gao, H. Peng, Z. Liu, D. Yu, E. Wang, Y. Jiang, F. Ding, K. Liu, *Adv. Mater.* **2018**, *30*, 1702944.
- [5] H. Gonzalez-Herrero, J. M. Gomez-Rodriguez, P. Mallet, M. Moaied, J. J. Palacios, C. Salgado, M. M. Ugeda, J. Y. Veuillen, F. Yndurain, I. Brihuega, *Science* **2016**, *352*, 437.
- [6] M. Wang, M. Tang, S. Chen, H. Ci, K. Wang, L. Shi, L. Lin, H. Ren, J. Shan, P. Gao, Z. Liu, H. Peng, *Adv. Mater.* **2017**, *29*, 1703882.
- [7] H. Wang, X. B. Li, L. Gao, H. L. Wu, J. Yang, L. Cai, T. B. Ma, C. H. Tung, L. Z. Wu, G. Yu, *Angew. Chem., Int. Ed.* **2018**, *57*, 192.
- [8] J. Ye, H. Tan, S. Wu, K. Ni, F. Pan, J. Liu, Z. Tao, Y. Qu, H. Ji, P. Simon, Y. Zhu, *Adv. Mater.* **2018**, *30*, 1801384.
- [9] Y. Hao, M. S. Bharathi, L. Wang, Y. Liu, H. Chen, S. Nie, X. Wang, H. Chou, C. Tan, B. Fallahazad, H. Ramanarayanan, C. W. Magnuson, E. Tutuc, B. I. Yakobson, K. F. McCarty, Y. W. Zhang, P. Kim, J. Hone, L. Colombo, R. S. Ruoff, *Science* **2013**, *342*, 720.
- [10] W. Guo, F. Jing, J. Xiao, C. Zhou, Y. Lin, S. Wang, *Adv. Mater.* **2016**, *28*, 3152.
- [11] L. Lin, J. Li, H. Ren, A. L. Koh, N. Kang, H. Peng, H. Q. Xu, Z. Liu, *ACS Nano* **2016**, *10*, 2922.
- [12] X. Xue, Q. Xu, H. Wang, S. Liu, Q. Jiang, Z. Yu, X. Zhou, T. Ma, L. Wang, G. Yu, *Chem. Mater.* **2019**, *31*, 1231.
- [13] M. Zeng, L. Wang, J. Liu, T. Zhang, H. Xue, Y. Xiao, Z. Qin, L. Fu, *J. Am. Chem. Soc.* **2016**, *138*, 7812.
- [14] L. Sun, L. Lin, Z. Wang, D. Rui, Z. Yu, J. Zhang, Y. Li, X. Liu, K. Jia, K. Wang, L. Zheng, B. Deng, T. Ma, N. Kang, H. Xu, K. S. Novoselov, H. Peng, Z. Liu, *Adv. Mater.* **2019**, *31*, 1902978.
- [15] K. Jia, J. Zhang, L. Lin, Z. Li, J. Gao, L. Sun, R. Xue, J. Li, N. Kang, Z. Luo, M. H. Rummeli, H. Peng, Z. Liu, *J. Am. Chem. Soc.* **2019**, *141*, 7670.
- [16] J. Zhang, K. ha, L. Lin, W. Zhao, Q. Huy Ta, L. Sun, T. Li, Z. Li, X. Liu, L. Zheng, R. Xue, J. Gao, Z. Luo, M. H. Rummeli, Q. Yuan, H. Peng, Z. Liu, *Angew. Chem., Int. Ed.* **2019**, *58*, 14446.
- [17] G. Yuan, D. Lin, Y. Wang, X. Huang, W. Chen, X. Xie, J. Zong, Q. Q. Yuan, H. Zheng, D. Wang, J. Xu, S. C. Li, Y. Zhang, J. Sun, X. Xi, L. Gao, *Nature* **2020**, *577*, 204.
- [18] T. Barkan, *Nat. Nanotechnol.* **2019**, *14*, 904.
- [19] L. Lin, H. Peng, Z. Liu, *Nat. Mater.* **2019**, *18*, 520.
- [20] S. Hu, M. Lozada-Hidalgo, F. C. Wang, A. Mishchenko, F. Schedin, R. R. Nair, E. W. Hill, D. W. Boukhvalov, M. I. Katsnelson, R. A. W. Dryfe, I. V. Grigorieva, H. A. Wu, A. K. Geim, *Nature* **2014**, *516*, 227.
- [21] A. Woessner, M. B. Lundeberg, Y. Gao, A. Principi, P. Alonso-Gonzalez, M. Carrega, K. Watanabe, T. Taniguchi, G. Vignale, M. Polini, J. Hone, R. Hillenbrand, F. H. L. Koppens, *Nat. Mater.* **2015**, *14*, 421.
- [22] A. K. Geim, I. V. Grigorieva, *Nature* **2013**, *499*, 419.
- [23] K. S. Novoselov, A. Mishchenko, A. Carvalho, A. H. Castro Neto, *Science* **2016**, *353*, aac9439.
- [24] N. Bultinck, S. Chatterjee, M. P. Zaletel, *Phys. Rev. Lett.* **2020**, *124*, 166601.
- [25] H. C. Po, L. Zou, A. Vishwanath, T. Senthil, *Phys. Rev. X* **2018**, *8*, 031089.
- [26] Y. Cao, J. Y. Luo, V. Fatemi, S. Fang, J. D. Sanchez-Yamagishi, K. Watanabe, T. Taniguchi, E. Kaxiras, P. Jarillo-Herrero, *Phys. Rev. Lett.* **2016**, *117*, 116804.
- [27] L. Ju, Z. Shi, N. Nair, Y. Ly, C. Jin, J. Velasco Jr., C. Ojeda-Aristizabal, H. A. Bechtel, M. C. Martin, A. Zettl, J. Analytis, F. Wang, *Nature* **2015**, *520*, 650.
- [28] I. Brihuega, P. Mallet, H. Gonzalez-Herrero, G. T. de laissardiere, M. M. Ugeda, L. Magaud, J. M. Gomez-Rodriguez, F. Yndurain, J. Y. Veuillen, *Phys. Rev. Lett.* **2012**, *109*, 196802.
- [29] J. B. Liu, P. J. Li, Y. F. Chen, Z.-G. Wang, F. Qi, J. R. He, B. J. Zheng, J. H. Zhou, W. L. Zhang, L. Gu, Y. R. Li, *Sci. Rep.* **2015**, *5*, 15285.
- [30] B. Fallahazad, Y. Hao, K. Lee, S. Kim, R. S. Ruoff, E. Tutuc, *Phys. Rev. B* **2012**, *85*, 201408.
- [31] L. Meng, Y. Zhang, W. Yan, L. Feng, L. He, R. F. Dou, J. C. Nie, *Appl. Phys. Lett.* **2012**, *100*, 091601.
- [32] J. H. Yoo, J. Bin In, J. Bok Park, H. Jeon, C. P. Grigoropoulos, *Appl. Phys. Lett.* **2012**, *100*, 233124.
- [33] P. S. Mahapatra, K. Sarkar, H. R. Krishnamurthy, S. Mukerjee, A. Ghosh, *Nano Lett.* **2017**, *17*, 6822.
- [34] X. Lu, P. Stepanov, W. Yang, M. Xie, M. A. Aamir, I. Das, C. Urgell, K. Watanabe, T. Taniguchi, G. Zhang, A. Bachtold, A. H. MacDonald, D. K. Efetov, *Nature* **2019**, *574*, 653.
- [35] G. Abbas, Y. Li, H. Wang, W. X. Zhang, C. Wang, H. Zhang, *Adv. Funct. Mater.* **2020**, *30*, 2000878.
- [36] J. Wang, X. Mu, L. Wang, M. Sun, *Mater. Today Phys.* **2019**, *9*, 100099.
- [37] A. Nimbalkar, H. Kim, *Nano-Micro Lett.* **2020**, *12*, 126.
- [38] K. Kim, A. DaSilva, S. Huang, B. Fallahazad, S. Larentis, T. Taniguchi, K. Watanabe, B. J. LeRoy, A. H. MacDonald, E. Tutuc, *Proc. Natl. Acad. Sci.* **2017**, *114*, 3364.
- [39] E. J. Mele, *Nature* **2018**, *556*, 37.
- [40] B. Padhi, C. Setty, P. W. Phillips, *Nano Lett.* **2018**, *18*, 6175.
- [41] G. Li, A. Luican, J. M. B. Lopes dos Santos, A. H. Castro Neto, A. Reina, J. Kong, E. Y. Andrei, *Nat. Phys.* **2010**, *6*, 109.
- [42] Z. D. Chu, W. Y. He, L. He, *Phys. Rev. B* **2013**, *87*, 155419.
- [43] W. Yao, E. Wang, C. Bao, Y. Zhang, K. Zhang, K. Bao, C. K. Chan, C. Chen, J. Avila, M. C. Asensio, J. Zhu, S. Zhou, *Proc. Natl. Acad. Sci.* **2018**, *115*, 6928.
- [44] B. Deng, B. Wang, N. Li, R. Li, Y. Wang, J. Tang, Q. Fu, Z. Tian, P. Gao, J. Xue, H. Peng, *ACS Nano* **2020**, *14*, 1656.
- [45] J. W. Jeon, H. Kim, H. Kim, S. Choi, B. H. Kim, *AIP Adv.* **2018**, *8*, 075228.
- [46] J. M. B. L. dos Santos, N. M. R. Peres, A. H. Castro Neto, *Phys. Rev. Lett.* **2007**, *99*, 256802.
- [47] Q. Yao, X. Chen, R. van Bremen, K. Sothewes, H. J. W. Zandvliet, *Appl. Phys. Lett.* **2020**, *116*, 011602.

- [48] C. Liu, X. Xu, L. Qiu, M. Wu, R. Qiao, L. Wang, J. Wang, J. Niu, J. Liang, X. Zhou, Z. Zhang, M. Peng, P. Gao, W. Wang, X. Bai, D. Ma, Y. Jiang, X. Wu, D. Yu, E. Wang, J. Xiong, F. Ding, K. Liu, *Nat. Chem.* **2019**, *11*, 730.
- [49] J. Dong, D. Geng, F. Liu, F. Ding, *Angew. Chem., Int. Ed.* **2019**, *58*, 7723.
- [50] J. Kim, H. Sakakita, H. Itagaki, *Nano Lett.* **2019**, *19*, 739.
- [51] Z. Chen, H. I. Wang, J. Teyssandier, K. S. Mali, T. Dumslaff, I. Ivanov, W. Zhang, P. Ruffieux, R. Fasel, H. J. Raeder, D. Turchinovich, S. De Feyter, X. Feng, M. Klæui, A. Narita, M. Bonn, K. Muellen, *J. Am. Chem. Soc.* **2017**, *139*, 3635.
- [52] J. Zeng, X. Ji, Y. Ma, Z. Zhang, S. Wang, Z. Ren, C. Zhi, J. Yu, *Adv. Mater.* **2018**, *30*, 1705380.
- [53] Y. Qi, B. Deng, X. Guo, S. Chen, J. Gao, T. Li, Z. Dou, H. Ci, J. Sun, Z. Chen, R. Wang, L. Cui, X. Chen, K. Chen, H. Wang, S. Wang, P. Gao, M. H. Rummeli, H. Peng, Y. Zhang, Z. Liu, *Adv. Mater.* **2018**, *30*, 1704839.
- [54] P. Solis-Fernandez, Y. Terao, K. Kawahara, W. Nishiyama, T. Uwanno, Y. C. Lin, K. Yamamoto, H. Nakashima, K. Nagashio, H. Hibino, K. Suenaga, H. Ago, *ACS Nano* **2020**, *14*, 6834.
- [55] Z. Qi, H. Shi, M. Zhao, H. Jin, S. Jin, X. Kong, R. S. Ruoff, S. Qin, J. Xue, H. Ji, *Chem. Mater.* **2018**, *30*, 7852.
- [56] J. Zhang, L. Lin, K. Jia, L. Sun, H. Peng, Z. Liu, *Adv. Mater.* **2020**, *32*, 1903266.
- [57] I. V. Vlassioulk, Y. Stehle, P. R. Pudasaini, R. R. Unocic, P. D. Rack, A. P. Baddorf, I. N. Ivanov, N. V. Lavrik, F. List, N. Gupta, K. V. Bets, B. I. Yakobson, S. N. Smirnov, *Nat. Mater.* **2018**, *17*, 318.
- [58] H. Patel, R. W. Havener, L. Brown, Y. Liang, L. Yang, J. Park, M. W. Graham, *Nano Lett.* **2015**, *15*, 5932.
- [59] H. W. Kim, J. Ku, W. Ko, Y. Cho, I. Jeon, S. W. Hwang, *J. Phys. Chem. C* **2017**, *121*, 24641.
- [60] T. Iwasaki, A. A. Zakharov, T. Eelbo, M. Waśniowska, R. Wiesendanger, J. H. Smet, U. Starke, *Surf. Sci.* **2014**, *625*, 44.
- [61] Y. Takesaki, K. Kawahara, H. Hibino, S. Okada, M. Tsuji, H. Ago, *Chem. Mater.* **2016**, *28*, 4583.
- [62] H. Q. Ta, D. J. Perello, D. L. Duong, G. H. Han, S. Gorantla, V. L. Nguyen, A. Bachmatiuk, S. V. Rotkin, Y. H. Lee, M. H. Rummeli, *Nano Lett.* **2016**, *16*, 6403.
- [63] B. Liu, Y. Sheng, S. Huang, Z. Guo, K. Ba, H. Yan, W. Bao, Z. Sun, *Chem. Mater.* **2019**, *31*, 6105.
- [64] X. Zhang, L. Wang, J. Xin, B. I. Yakobson, F. Ding, *J. Am. Chem. Soc.* **2014**, *136*, 3040.
- [65] W. Ma, M. L. Chen, L. Yin, Z. Liu, H. Li, C. Xu, X. Xin, D. M. Sun, H. M. Cheng, W. Ren, *Nat. Commun.* **2019**, *10*, 2809.
- [66] J. Kozlova, A. Niilisk, H. Alles, V. Sammelselg, *Carbon* **2015**, *94*, 160.
- [67] Q. Li, H. Chou, J. H. Zhong, J. Y. Liu, A. Dolocan, J. Zhang, Y. Zhou, R. S. Ruoff, S. Chen, W. Cai, *Nano Lett.* **2013**, *13*, 486.
- [68] Z. Peng, Z. Yan, Z. Sun, J. M. Tour, *ACS Nano* **2011**, *5*, 8241.
- [69] B. Luo, B. Chen, A. Wang, D. Geng, J. Xu, H. Wang, Z. Zhang, L. Peng, Z. Xu, G. Yu, *J. Mater. Chem. C* **2016**, *4*, 7464.
- [70] M. S. Dresselhaus, G. Dresselhaus, K. Sugihara, I. L. Spain, H. A. Goldberg, *Adv. Mater.* **1989**, *1*, 130.
- [71] Z. Yan, Y. Liu, L. Ju, Z. Peng, J. Lin, G. Wang, H. Zhou, C. Xiang, E. L. Samuel, C. Kittrell, V. I. Artyukhov, F. Wang, B. I. Yakobson, J. M. Tour, *Angew. Chem., Int. Ed. Engl.* **2014**, *53*, 1565.
- [72] Z. Gao, Q. Zhang, C. H. Naylor, Y. Kim, I. H. Abidi, J. Ping, P. Ducos, J. Zauberman, M. Q. Zhao, A. M. Rappe, Z. Luo, L. Ren, A. T. C. Johnson, *ACS Nano* **2018**, *12*, 2275.
- [73] X. Li, W. Cai, J. An, S. Kim, J. Nah, D. Yang, R. Piner, A. Velamakanni, I. Jung, E. Tutuc, S. K. Banerjee, L. Colombo, R. S. Ruoff, *Science* **2009**, *324*, 1312.
- [74] M. Huang, R. S. Ruoff, *Acc. Chem. Res.* **2020**, *53*, 800.
- [75] M. Huang, M. Biswal, H. J. Park, S. Jin, D. Qu, S. Hong, Z. Zhu, L. Qiu, D. Luo, X. Liu, Z. Yang, Z. Liu, Y. Huang, H. Lim, W. J. Yoo, F. Ding, Y. Wang, Z. Lee, R. S. Ruoff, *ACS Nano* **2018**, *12*, 6117.
- [76] C. C. Lu, Y. C. Lin, Z. Liu, C. H. Yeh, K. Suenaga, P. W. Chiu, *ACS Nano* **2013**, *7*, 2587.
- [77] H. Wang, X. Xue, Q. Jiang, Y. Wang, D. Geng, L. Cai, L. Wang, Z. Xu, G. Yu, *J. Am. Chem. Soc.* **2019**, *141*, 11004.
- [78] H. C. Lee, S. B. Jo, E. Lee, M. S. Yoo, H. H. Kim, S. K. Lee, W. H. Lee, K. Cho, *Adv. Mater.* **2016**, *28*, 2010.
- [79] H. Shi, Z. Zhan, Z. Qi, K. Huang, E. van Veen, J. A. Silva-Guillen, R. Zhang, P. Li, K. Xie, H. Ji, M. I. Katsnelson, S. Yuan, S. Qin, Z. Zhang, *Nat. Commun.* **2020**, *11*, 371.
- [80] R. W. Havener, H. Zhuang, L. Brown, R. G. Hennig, J. Park, *Nano Lett.* **2012**, *12*, 3162.
- [81] R. He, T. F. Chung, C. Delaney, C. Keiser, L. A. Jauregui, P. M. Shand, C. C. Chancey, Y. Wang, J. Bao, Y. P. Chen, *Nano Lett.* **2013**, *13*, 3594.
- [82] L. Liu, H. Zhou, R. Cheng, W. J. Yu, Y. Liu, Y. Chen, J. Shaw, X. Zhong, Y. Huang, X. Duan, *ACS Nano* **2012**, *6*, 8241.
- [83] P. Solis-Fernandez, Y. Terao, K. Kawahara, W. Nishiyama, T. Uwanno, Y. C. Lin, K. Yamamoto, H. Nakashima, K. Nagashio, H. Hibino, K. Suenaga, H. Ago, *ACS Nano* **2020**, *14*, 6834.
- [84] M. Huang, P. V. Bakharev, Z. J. Wang, M. Biswal, Z. Yang, S. Jin, B. Wang, H. J. Park, Y. Li, D. Qu, Y. Kwon, X. Chen, S. H. Lee, M. G. Willinger, W. J. Yoo, Z. Lee, R. S. Ruoff, *Nat. Nanotechnol.* **2020**, *15*, 289.
- [85] V. L. Nguyen, D. L. Duong, S. H. Lee, J. Avila, G. Han, Y. M. Kim, M. C. Asensio, S. Y. Jeong, Y. H. Lee, *Nat. Nanotechnol.* **2020**, *15*, 861.
- [86] J. Kim, H. Park, J. B. Hannon, S. W. Bedell, K. Fogel, D. K. Sadana, C. Dimitrakopoulos, *Science* **2013**, *342*, 833.
- [87] L. A. Galves, J. M. Wofford, G. V. Soares, U. Jahn, C. Pfüller, H. Riechert, J. M. J. Lopes, *Carbon* **2017**, *115*, 162.
- [88] Y. Jia, L. Guo, J. Lin, J. Yang, X. Chen, *Carbon* **2017**, *114*, 585.
- [89] S. J. Ahn, P. Moon, T. H. Kim, H. W. Kim, H. C. Shin, E. H. Kim, H. W. Cha, S. J. Kahng, P. Kim, M. Koshino, Y. W. Son, C. W. Yang, J. R. Ahn, *Science* **2018**, *361*, 782.
- [90] H. Kageshima, H. Hibino, S. Tanabe, *J. Phys.: Condens. Matter* **2012**, *24*, 314215.
- [91] T. Suzuki, T. Iimori, S. J. Ahn, Y. Zhao, M. Watanabe, J. Xu, M. Fujisawa, T. Kanai, N. Ishii, J. Itatani, K. Suwa, H. Fukidome, S. Tanaka, J. R. Ahn, K. Okazaki, S. Shin, F. Komori, I. Matsuda, *ACS Nano* **2019**, *13*, 11981.
- [92] K. Kim, S. Coh, L. Z. Tan, W. Regan, J. M. Yuk, E. Chatterjee, M. F. Crommie, M. L. Cohen, S. G. Louie, A. Zettl, *Phys. Rev. Lett.* **2012**, *108*, 246103.
- [93] S. Fan, Q. A. Vu, M. D. Tran, S. Adhikari, Y. H. Lee, *2D Mater.* **2020**, *7*, 022005.
- [94] P. Rickhaus, J. Wallbank, S. Slizovskiy, R. Pisoni, H. Overweg, Y. Lee, M. Eich, M. H. Liu, K. Watanabe, T. Taniguchi, T. Ihn, K. Ensslin, *Nano Lett.* **2018**, *18*, 6725.
- [95] R. Frisenda, E. Navarro-Moratalla, P. Gant, D. Perez De Lara, P. Jarillo-Herrero, R. V. Gorbachev, A. Castellanos-Gomez, *Chem. Soc. Rev.* **2018**, *47*, 53.
- [96] N. Mishra, S. Forti, F. Fabbri, L. Martini, C. McAleese, B. R. Conran, P. R. Whelan, A. Shivayogimath, B. S. Jessen, L. Buss, J. Falta, I. Aliaj, S. Roddar, J. I. Flege, P. Boggild, K. B. K. Teo, C. Coletti, *Small* **2019**, *15*, 1904906.
- [97] S. Wei, L. P. Ma, M. L. Chen, Z. Liu, W. Ma, D. M. Sun, H. M. Cheng, W. Ren, *Carbon* **2019**, *148*, 241.
- [98] M. Yi, Z. Shen, *J. Mater. Chem. A* **2015**, *3*, 11700.
- [99] X. D. Chen, W. Xin, W. S. Jiang, Z. B. Liu, Y. Chen, J. G. Tian, *Adv. Mater.* **2016**, *28*, 2563.
- [100] K. Kim, M. Yankowitz, B. Fallahazad, S. Kang, H. C. Movva, S. Huang, S. Larentis, C. M. Corbet, T. Taniguchi, K. Watanabe, S. K. Banerjee, B. J. LeRoy, E. Tutuc, *Nano Lett.* **2016**, *16*, 1989.

- [101] X. Yang, X. Li, Y. Deng, Y. Wang, G. Liu, C. Wei, H. Li, Z. Wu, Q. Zheng, Z. Chen, Q. Jiang, H. Lu, J. Zhu, *Adv. Funct. Mater.* **2019**, *29*, 1902427.
- [102] G. F. Schneider, V. E. Calado, H. Zandbergen, L. M. K. Vandersypen, C. Dekker, *Nano Lett.* **2010**, *10*, 1912.
- [103] Z. Tan, J. Yin, C. Chen, H. Wang, L. Lin, L. Sun, J. Wu, X. Sun, H. Yang, Y. Chen, H. Peng, Z. Liu, *ACS Nano* **2016**, *10*, 6725.
- [104] Y. Wang, S. W. Tong, X. F. Xu, B. Ozylmaz, K. P. Loh, *Adv. Mater.* **2011**, *23*, 1514.
- [105] Y. C. Lin, C. C. Lu, C. H. Yeh, C. Jin, K. Suenaga, P. W. Chiu, *Nano Lett.* **2012**, *12*, 414.
- [106] M. Her, R. Beams, L. Novotny, *Phys. Lett. A* **2013**, *377*, 1455.
- [107] H. Sun, D. Chen, Y. Wu, Q. Yuan, L. Guo, D. Dai, Y. Xu, P. Zhao, N. Jiang, C. T. Lin, *J. Mater. Chem. C* **2017**, *5*, 1880.
- [108] A. L. Sharpe, E. J. Fox, A. W. Barnard, J. Finney, K. Watanabe, T. Taniguchi, M. A. Kastner, D. Goldhaber-Gordon, *Science* **2019**, *365*, 605.
- [109] C. R. Dean, A. F. Young, I. Meric, C. Lee, L. Wang, S. Sorgenfrei, K. Watanabe, T. Taniguchi, P. Kim, K. L. Shepard, J. Hone, *Nat. Nanotechnol.* **2010**, *5*, 722.
- [110] H. Imamura, A. Visikovskiy, R. Uotani, T. Kajiwara, H. Ando, T. Iimori, K. Iwata, T. Miyamachi, K. Nakatsuji, K. Mase, T. Shirasawa, F. Komori, S. Tanaka, *Appl. Phys. Express* **2020**, *13*, 075004.
- [111] Z. Ni, Y. Wang, T. Yu, Y. You, Z. Shen, *Phys. Rev. B* **2008**, *77*, 235403.
- [112] S. Akcoeltekin, H. Bukowska, T. Peters, O. Osmani, I. Monnet, I. Alzaher, B. B. d'Etat, H. Lebius, M. Schleberger, *Appl. Phys. Lett.* **2011**, *98*, 103103.
- [113] H. Schmidt, J. C. Rode, D. Smirnov, R. J. Haug, *Nat. Commun.* **2014**, *5*, 5742.
- [114] V. Carozo, C. M. Almeida, B. Fragneaud, P. M. Bedê, M. V. O. Moutinho, J. Ribeiro-Soares, N. F. Andrade, A. G. Souza Filho, M. J. S. Matos, B. Wang, M. Terrones, R. B. Capaz, A. Jorio, C. A. Achete, L. G. Cançado, *Phys. Rev. B* **2013**, *88*, 085401.
- [115] H. Chen, X. L. Zhang, Y. Y. Zhang, D. Wang, D. L. Bao, Y. Que, W. Xiao, S. Du, M. Ouyang, S. T. Pantelides, H. J. Gao, *Science* **2019**, *365*, 1036.
- [116] B. Wang, M. Huang, N. Y. Kim, B. V. Cunning, Y. Huang, D. Qu, X. Chen, S. Jin, M. Biswal, X. Zhang, S. H. Lee, H. Lim, W. J. Yoo, Z. Lee, R. S. Ruoff, *Nano Lett.* **2017**, *17*, 1467.
- [117] E. Khestanova, F. Guinea, L. Fumagalli, A. K. Geim, I. V. Grigorieva, *Nat. Commun.* **2016**, *7*, 12587.
- [118] D. A. Sanchez, Z. Dai, P. Wang, A. Cantu-Chavez, C. J. Brennan, R. Huang, N. Lu, *Proc. Natl. Acad. Sci.* **2018**, *115*, 7884.
- [119] Z. Dai, N. Lu, K. M. Liechti, R. Huang, *Curr. Opin. Solid State Mater. Sci.* **2020**, *24*, 100837.
- [120] M. R. Rosenberger, H. J. Chuang, K. M. McCreary, A. T. Hanbicki, S. V. Sivaram, B. T. Jonker, *ACS Appl. Mater. Interfaces* **2018**, *10*, 10379.
- [121] S. Wakolbinger, F. R. Geisenhof, F. Winterer, S. Palmer, J. G. Crimmann, K. Watanabe, T. Taniguchi, F. Trixler, R. T. Weitz, *2D Mater.* **2020**, *7*, 035002.
- [122] D. G. Purdie, N. M. Pugno, T. Taniguchi, K. Watanabe, A. C. Ferrari, A. Lombardo, *Nat. Commun.* **2018**, *9*, 5387.
- [123] Y. Cao, D. Rodan-Legrain, O. Rubies-Bigorda, J. M. Park, K. Watanabe, T. Taniguchi, P. Jarillo-Herrero, *Nature* **2020**, *583*, 215.
- [124] F. Pizzocchero, L. Gammelgaard, B. S. Jessen, J. M. Caridad, L. Wang, J. Hone, P. Boggild, T. J. Booth, *Nat. Commun.* **2016**, *7*, 11894.
- [125] Y. Bai, L. Zhou, J. Wang, W. Wu, L. J. McGilly, D. Halbertal, C. F. B. Lo, F. Liu, J. Ardelean, P. Rivera, N. R. Finney, X. C. Yang, D. N. Basov, W. Yao, X. Xu, J. Hone, A. N. Pasupathy, X. Y. Zhu, *Nat. Mater.* **2020**, *19*, 1068.
- [126] N. P. Kazmierczak, M. Van Winkle, C. Ophus, K. C. Bustillo, H. G. Brown, S. Carr, J. Ciston, T. Taniguchi, K. Watanabe, D. Kwabena Bediako, arXiv:2008.09761, **2020**.
- [127] W. Yan, W. Y. He, Z. D. Chu, M. Liu, L. Meng, R. F. Dou, Y. Zhang, Z. Liu, J. C. Nie, L. He, *Nat. Commun.* **2013**, *4*, 2159.
- [128] J. Mao, S. P. Milovanovic, M. Andelkovic, X. Lai, Y. Cao, K. Watanabe, T. Taniguchi, L. Covaci, F. M. Peeters, A. K. Geim, Y. Jiang, E. Y. Andrei, *Nature* **2020**, *584*, 215.
- [129] Y. C. Chen, W. H. Lin, W. S. Tseng, C. C. Chen, G. R. Rossman, C. D. Chen, Y. S. Wu, N. C. Yeh, *Carbon* **2020**, *156*, 212.
- [130] T. Latychevskaia, C. Escher, H. W. Fink, *Ultramicroscopy* **2019**, *197*, 46.
- [131] S. Pezzini, V. Miseikis, G. Piccinini, S. Forti, S. Pace, R. Engelke, F. Rossella, K. Watanabe, T. Taniguchi, P. Kim, C. Coletti, *Nano Lett.* **2020**, *20*, 3313.
- [132] I. Razado-Colambo, J. Avila, J. P. Nys, C. Chen, X. Wallart, M. C. Asensio, D. Vignaud, *Sci. Rep.* **2016**, *6*, 27261.
- [133] V. Carozo, C. M. Almeida, E. H. Ferreira, L. G. Cancado, C. A. Achete, A. Jorio, *Nano Lett.* **2011**, *11*, 4527.
- [134] Y. Chen, L. Meng, W. Zhao, Z. Liang, X. Wu, H. Nan, Z. Wu, S. Huang, L. Sun, J. Wang, Z. Ni, *Phys. Chem. Chem. Phys.* **2014**, *16*, 21682.
- [135] G. W. Burg, J. Zhu, T. Taniguchi, K. Watanabe, A. H. MacDonald, E. Tutuc, *Phys. Rev. Lett.* **2019**, *123*, 197702.
- [136] F. Wu, S. Das Sarma, *Phys. Rev. Lett.* **2020**, *124*, 046403.
- [137] A. H. Castro Neto, F. Guinea, N. M. R. Peres, K. S. Novoselov, A. K. Geim, *Rev. Mod. Phys.* **2009**, *81*, 109.
- [138] Y. Cao, V. Fatemi, S. Fang, K. Watanabe, T. Taniguchi, E. Kaxiras, P. Jarillo-Herrero, *Nature* **2018**, *556*, 43.
- [139] M. Yankowitz, S. Chen, H. Polshyn, Y. Zhang, K. Watanabe, T. Taniguchi, D. Graf, A. F. Young, C. R. Dean, *Science* **2019**, *363*, 1059.
- [140] H. S. Arora, R. Polski, Y. Zhang, A. Thomson, Y. Choi, H. Kim, Z. Lin, I. Z. Wilson, X. Xu, J. H. Chu, K. Watanabe, T. Taniguchi, J. Alicea, S. Nadj-Perge, *Nature* **2020**, *583*, 379.
- [141] C. Shen, Y. Chu, Q. Wu, N. Li, S. Wang, Y. Zhao, J. Tang, J. Liu, J. Tian, K. Watanabe, T. Taniguchi, R. Yang, Z. Y. Meng, D. Shi, O. V. Yazyev, G. Zhang, *Nat. Phys.* **2020**, *16*, 520.
- [142] M. Koshino, *Phys. Rev. B* **2019**, *99*, 235406.
- [143] J. Y. Lee, E. Khalaf, S. Liu, X. Liu, Z. Hao, P. Kim, A. Vishwanath, *Nat. Commun.* **2019**, *10*, 5333.
- [144] F. Haddadi, Q. Wu, A. J. Kruchkov, O. V. Yazyev, *Nano Lett.* **2020**, *20*, 2410.
- [145] G. Chen, A. L. Sharpe, P. Gallagher, I. T. Rosen, E. J. Fox, L. Jiang, B. Lyu, H. Li, K. Watanabe, T. Taniguchi, J. Jung, Z. Shi, D. Goldhaber-Gordon, Y. Zhang, F. Wang, *Nature* **2019**, *572*, 215.
- [146] W. Y. He, D. Goldhaber-Gordon, K. T. Law, *Nat. Commun.* **2020**, *11*, 1650.
- [147] F. Wu, S. D. Sarma, *Phys. Rev. B* **2020**, *101*, 155149.
- [148] C. Repellin, Z. Dong, Y. H. Zhang, T. Senthil, *Phys. Rev. Lett.* **2020**, *124*, 187601.
- [149] M. Lamparski, B. Van Troeye, V. Meunier, *2D Mater.* **2020**, *7*, 025050.
- [150] L. Jiang, Z. Shi, B. Zeng, S. Wang, J. H. Kang, T. Joshi, C. Jin, L. Ju, J. Kim, T. Lyu, Y. R. Shen, M. Crommie, H. J. Gao, F. Wang, *Nat. Mater.* **2016**, *15*, 840.
- [151] L. Ju, Z. Shi, N. Nair, Y. Lv, C. Jin, J. VelascoJr., C. Ojeda-Aristizabal, H. A. Bechtel, M. C. Martin, A. Zettl, J. Analytis, F. Wang, *Nature* **2015**, *520*, 650.
- [152] L. Jiang, S. Wang, S. Zhao, M. Crommie, F. Wang, *Nano Lett.* **2020**, *20*, 5936.
- [153] W. Yan, M. Liu, R.-F. Dou, L. Meng, L. Feng, Z. D. Chu, Y. Zhang, Z. Liu, J. C. Nie, L. He, *Phys. Rev. Lett.* **2012**, *109*, 126801.
- [154] R. Othmen, H. Arezki, H. Ajlani, A. Cavanna, M. Bouthchich, M. Oueslati, A. Madouri, *Appl. Phys. Lett.* **2015**, *106*, 103107.
- [155] Y. Ding, Q. Peng, L. Gan, R. Wu, X. Ou, Q. Zhang, Z. Luo, *Chem. Mater.* **2016**, *28*, 1034.
- [156] J. Yin, H. Wang, H. Peng, Z. Tan, L. Liao, L. Lin, X. Sun, A. L. Koh, Y. Chen, H. Peng, Z. Liu, *Nat. Commun.* **2016**, *7*, 10699.
- [157] H. Patel, L. Huang, C. J. Kim, J. Park, M. W. Graham, *Nat. Commun.* **2019**, *10*, 1445.

- [158] L. Liao, H. Wang, H. Peng, J. Yin, A. L. Koh, Y. Chen, Q. Xie, H. Peng, Z. Liu, *Nano Lett.* **2015**, *15*, 5585.
- [159] B. Deng, C. Ma, Q. Wang, S. Yuan, K. Watanabe, T. Taniguchi, F. Zhang, F. Xia, *Nat. Photonics* **2020**, *14*, 549.
- [160] E. V. Castro, K. S. Novoselov, S. V. Morozov, N. M. Peres, J. M. dos Santos, J. Nilsson, F. Guinea, A. K. Geim, A. H. Neto, *Phys. Rev. Lett.* **2007**, *99*, 216802.
- [161] T. Taychatanapat, P. Jarillo-Herrero, *Phys. Rev. Lett.* **2010**, *105*, 166601.
- [162] Y. Hao, L. Wang, Y. Liu, H. Chen, X. Wang, C. Tan, S. Nie, J. W. Suk, T. Jiang, T. Liang, J. Xiao, W. Ye, C. R. Dean, B. I. Yakobson, K. F. McCarty, P. Kim, J. Hone, L. Colombo, R. S. Ruoff, *Nat. Nanotechnol.* **2016**, *11*, 426.
- [163] N. N. T. Nam, M. Koshino, *Phys. Rev. B* **2017**, *96*, 075311.
- [164] T. F. Chung, Y. Xu, Y. P. Chen, *Phys. Rev. B* **2018**, *98*, 035425.
- [165] H. Polshyn, M. Yankowitz, S. Chen, Y. Zhang, K. Watanabe, T. Taniguchi, C. R. Dean, A. F. Young, *Nat. Phys.* **2019**, *15*, 1011.
- [166] P. Rickhaus, G. Zheng, J. L. Lado, Y. Lee, A. Kurzmann, M. Eich, R. Pisoni, C. Tong, R. Garreis, C. Gold, M. Masseroni, T. Taniguchi, K. Wantanabe, T. Ihn, K. Ensslin, *Nano Lett.* **2019**, *19*, 8821.
- [167] Y. Zhang, T. T. Tang, C. Girit, Z. Hao, M. C. Martin, A. Zettl, M. F. Crommie, Y. R. Shen, F. Wang, *Nature* **2009**, *459*, 820.
- [168] D. De Fazio, D. G. Purdie, A. K. Ott, P. Braeuninger-Weimer, T. Khodkov, S. Goossens, T. Taniguchi, K. Watanabe, P. Livreri, F. H. L. Koppens, S. Hofmann, I. Goykhman, A. C. Ferrari, A. Lombardo, *ACS Nano* **2019**, *13*, 8926.
- [169] W. Kong, H. Kum, S. H. Bae, J. Shim, H. Kim, L. Kong, Y. Meng, K. Wang, C. Kim, J. Kim, *Nat. Nanotechnol.* **2019**, *14*, 927.
- [170] J. Park, W. C. Mitchel, S. Elhamri, L. Grazulis, J. Hoelscher, K. Mahalingam, C. Hwang, S. K. Mo, J. Lee, *Nat. Commun.* **2015**, *6*, 5677.
- [171] L. Cai, G. Yu, *Small Methods* **2019**, *3*, 1900071.
- [172] E. Lee, K. A. Persson, *Nano Lett.* **2012**, *12*, 4624.
- [173] K. Ji, J. Han, A. Hirata, T. Fujita, Y. Shen, S. Ning, P. Liu, H. Kashani, Y. Tian, Y. Ito, J. I. Fujita, Y. Oyama, *Nat. Commun.* **2019**, *10*, 275.
- [174] D. T. Larson, S. Carr, G. A. Tritsaris, E. Kaxiras, *Phys. Rev. B* **2020**, *101*, 075407.



**Le Cai** received her B.S. from the College of Chemistry, Xiangtan University, in 2005. Presently, she is working for her Ph.D. degree at the Institute of Chemistry, Chinese academy of Sciences, under the instruction of Prof. Yu. Her main research interest is the growth of 2D conjugated polymers through chemical vapor deposition (like graphene and covalent organic framework) and their applications in electrical-related or energy-related field.



**Gui Yu** is currently a professor at the Institute of chemistry, Chinese Academy of Science. He graduated from Jilin University in 1988 and received his M.S. (1993) and Ph.D. (1997) degrees from Changchun institute of Physics, Chinese Academy of Science. After obtaining his Ph.D., he worked as a postdoctoral fellow in the Institute of chemistry. Thereafter, he was appointed to the position of associate professor in 1999 and promoted to professor in 2008. His current research mainly focuses on the synthesis of organic/polymers, graphene, covalent organic frameworks, and optoelectronic devices of these materials.